JGR Atmospheres

RESEARCH ARTICLE
10.1029/2025JD044623

Key Points:

- Warm-season soil NO_x emissions (SNO_x) account for 23%–27% of total NO_x emissions in China during 2015–2022
- As anthropogenic emissions decline, SNO_x changes can promote the increase in warm-season O_3 concentrations
- O_3 pollution control must consider both soil and anthropogenic NO_x emissions and take into account regional and seasonal differences

Supporting Information:

Supporting Information may be found in the online version of this article.

Correspondence to:

T. Sha,
tong-sha@sust.edu.cn

Citation:

Sha, T., Yang, S., Chen, Q., Wei, J., Ma, M., Gao, Y., et al. (2025). Elucidating contributions of anthropogenic and soil NO_x emissions changes to O_3 trends over China. *Journal of Geophysical Research: Atmospheres*, *130*, e2025JD044623. https://doi.org/10.1029/2025JD044623

Received 17 JUN 2025
Accepted 18 OCT 2025

Author Contributions:

Conceptualization: Tong Sha, K. Folkert Boersma, Jun Wang
Data curation: Jing Wei
Formal analysis: Tong Sha, Siyu Yang
Funding acquisition: Tong Sha
Investigation: Tong Sha, Siyu Yang
Methodology: Tong Sha, Siyu Yang
Resources: Mingchen Ma, Yufan Zhu, Yan Hu
Supervision: Qingcai Chen
Visualization: Siyu Yang
Writing – original draft: Tong Sha, Siyu Yang
Writing – review & editing: Tong Sha, Siyu Yang, Qingcai Chen, Jing Wei, Yang Gao, K. Folkert Boersma, Jun Wang

Elucidating Contributions of Anthropogenic and Soil NO_x Emissions Changes to O_3 Trends Over China

Tong Sha[1,2], Siyu Yang[1,2], Qingcai Chen[1], Jing Wei[3], Mingchen Ma[4], Yang Gao[5], Yufan Zhu[2], Yan Hu[2], K. Folkert Boersma[6,7], and Jun Wang[8]

[1]Shaanxi University Key Laboratory of Industrial Pollution Control and Environmental Health, School of Environmental Science and Engineering, Shaanxi University of Science & Technology, Xi'an, China, [2]Shaanxi Key Laboratory of Environmental Monitoring and Forewarning of Trace Pollution, Xi'an, China, [3]MEEKL-AERM, College of Environmental Sciences and Engineering, Institute of Tibetan Plateau, and Center for Environment and Health, Peking University, Beijing, China, [4]State Key Joint Laboratory of Environmental Simulation and Pollution Control, School of Environment, Tsinghua University, Beijing, China, [5]Frontiers Science Center for Deep Ocean Multispheres and Earth System and Key Laboratory of Marine Environmental Science and Ecology, Ministry of Education, Ocean University of China, and Laoshan Laboratory, Qingdao, China, [6]Meteorology and Air Quality, Wageningen University, Wageningen, The Netherlands, [7]Satellite Observations Department, Royal Netherlands Meteorological Institute, De Bilt, The Netherlands, [8]Department of Chemical and Biochemical Engineering, Center for Global and Regional Environmental Research, and Iowa Technology Institute, University of Iowa, Iowa City, IA, USA

Abstract Surface ozone (O_3) pollution is a critical environmental challenge, but existing research predominantly focuses on its summer peaks. Our analysis shows that high-O_3 episodes now expand into spring and autumn in China, with warm-season (April–September) maximum daily average 8-hr (MDA8) O_3 concentrations rising at 5.2 μg m^{-3} yr^{-1} during 2014–2023. Current O_3 mitigation focuses on anthropogenic NO_x emissions (ANO_x) while neglecting the contribution of soil NO_x emissions (SNO_x) to tropospheric O_3 formation. Here, we developed an innovative framework combining the machine learning model (XGBoost) with the Unified Inputs for WRF-Chem (UI-WRF-Chem) to quantify the impacts of ANO_x and SNO_x on O_3 increases during 2015–2019. Results show that although warm-season SNO_x constitute only 23%–27% of total NO_x emissions in China (2015–2022), they generally drive O_3 increases, exhibiting distinct regional and seasonal heterogeneities. Compared to urban areas, the O_3 formation regimes in rural areas of the Yangtze River Delta region predominantly shift to NO_x-limited, making O_3 highly sensitive to SNO_x. SNO_x changes lead to warm-season MDA8 O_3 increases of 1.0–1.3 μg m^{-3} during 2016–2019 relative to 2015. Although similar regime shifts have occurred, rural areas in the Beijing-Tianjin-Hebei and Fenwei Plain regions still retain strong VOCs-limited characteristics; thus, SNO_x perturbation impacts on O_3 are smaller. Although summer SNO_x are higher, their contribution to O_3 increases in transitional seasons (April, May, and September) shows an upward trend, suggesting more attention should be paid to fertilization-driven SNO_x. Our study highlights that future O_3 control strategies should account for SNO_x and their regional and seasonal differences.

Plain Language Summary Surface ozone (O_3) pollution in China is no longer confined to summer. Our study reveals that high-O_3 episodes have extended into spring and autumn, with concentrations increasing significantly each year. While strategies to reduce anthropogenic NO_x emissions (ANO_x) remain crucial for O_3 mitigation, our study highlights the underappreciated role of soil NO_x emissions (SNO_x), which constitute 23%–27% of total NO_x during warm seasons (April–September) in China. In this study, we employed an innovative approach combining machine learning and a numerical model to assess the impacts of ANO_x and SNO_x on warm-season O_3 increases from 2015 to 2019. Our simulations suggest that SNO_x can exacerbate O_3 pollution across China, and its impact varies by region and season. Notably, fertilization-driven SNO_x contribute to rising O_3 levels, even though soil emission levels are lower than in summer. As China successfully reduces industrial and vehicle emissions, O_3 formation is likely to become more sensitive to SNO_x. Our findings highlight the importance for policymakers to develop tailored, season-specific strategies for controlling soil emissions to effectively mitigate O_3 pollution.

1. Introduction

Surface ozone (O_3) is an emerging air pollution problem in China. Long-term exposure to O_3 pollution can pose a considerable threat to human health and exert substantial impacts on terrestrial ecosystems, agricultural yields, and climate change (Li, Gao, et al., 2024; Wang, Lin, et al., 2022; Zhang, Xu, et al., 2022). Tropospheric O_3 primarily generates from photochemical reactions of nitrogen oxides ($NO_x = NO + NO_2$) and volatile organic compounds (VOCs) (Roelofs & Lelieveld, 1997; Wang et al., 2017). Since 2013, the Chinese government has implemented a series of air pollution control measures that have effectively reduced anthropogenic NO_x (ANO_x) and particulate matter emissions, leading to $PM_{2.5}$ pollution mitigation (Li et al., 2019a, 2019b), but the surface O_3 concentrations still increased over the past decade (Liu et al., 2023). Many studies attribute the O_3 increase to the changes in meteorological conditions, precursor emissions, and climate change (Ni et al., 2024; Yang et al., 2024; Yao et al., 2024), specifically reductions in anthropogenic emissions and weakening of aerosol radiative effects (Li et al., 2020; Ma et al., 2020; Wang, Huang, et al., 2022).

There is a nonlinear relationship between photochemically generated O_3 and its precursors, including NO_x and VOCs (Hou et al., 2022; Jiang et al., 2022). These precursors are emitted from anthropogenic sources (e.g., fuel combustion from power plants and industry, transportation, and residential) and natural sources (e.g., soils, biomass burning, and lightning) (Ding et al., 2021; Huber et al., 2020; Lu et al., 2021). A recent study found that continuous decreases in ANO_x have effectively reduced tropospheric NO_2 vertical column densities (NO_2 columns) in urban areas of China during summer 2011–2023, while NO_2 columns in rural areas showed slower changes and even displayed a stabilized or slight increase in some natural areas (Wang et al., 2024). This discrepancy suggests that the NO_2 budget in rural areas may be more influenced by natural sources. NO_x emissions from soils, accounting for 12%–20% of global NO_x emissions (Vinken et al., 2014; Yan et al., 2005), are dynamically controlled by diverse factors, such as meteorological factors, soil temperature and moisture, available nitrogen content in soils, and agricultural practices. Despite the influences from natural nitrogen pool and agricultural fertilizer input, which are to some extent human-controlled, soil NO_x emissions (SNO_x) are conventionally considered as a natural source and overlooked in the current air pollution control strategies.

Chemical transport models (CTMs), such as WRF-Chem, WRF-CMAQ, and GEOS-Chem, have become increasingly popular in addressing O_3-related issues in China (Zhang et al., 2023), providing insights into understanding the role of local emissions and regional transport (Wang, Wang, et al., 2022; Zhang, Yu, et al., 2022), contributions of specific emission sources (Liu, Ma, et al., 2020), and policy effectiveness (Liu et al., 2023). By using CTMs, previous studies found that SNO_x in agricultural areas of China can increase summer O_3 concentrations by 5%–32% (Sha et al., 2024; Wang, Bei, et al., 2022; Wang, et al., 2024). However, previous CTM studies mainly focus on the impact of SNO_x on summer O_3 pollution in individual months (typically from June to August), with limited attention paid to the specific contribution of SNO_x to long-term O_3 variations. Since CTMs rely on simplifications of complex chemical mechanisms and physical processes, they are subject to uncertainties in parameterization schemes as well as inaccuracies in input data (e.g., meteorological and emission data), making it challenging to reproduce long-term trends and short-term variations in O_3 across China, particularly near the surface (Lu et al., 2025). This leads to uncertainties in the attribution of O_3 trends based on CTMs (Huang et al., 2021, 2025).

Compared with CTMs, machine learning (ML) methods, such as random forest, extreme gradient boosting, and light gradient boosting, have the advantages of computational efficiency. These approaches only require certain key predictors (e.g., meteorological variables and precursor emissions, etc.) to establish statistical models for O_3 concentrations (Hou et al., 2022; Zhu et al., 2023). Moreover, they are more proficient and efficient in dealing with nonlinear problems and thus have been widely applied to predict O_3 levels (Kuo & Fu, 2023; Ning et al., 2024). However, most ML methods are fundamentally black-box models, with inherent drawbacks of limited interpretability and lack of physicochemical mechanisms (Hou et al., 2022). The recently developed Shapley Additive Explanations (SHAP) technique provides a framework for quantifying the importance and interactions of multidimensional features, thereby solving some of the black-box limitations in ML. Although many studies have used the SHAP method to reveal the driving factors of particulate matter and O_3 pollution (Cheng et al., 2023; Zhang et al., 2024), it is worth noting that, unlike CTMs, the SHAP-based ML approach still cannot quantify the specific contributions of driving factors to O_3 formation, but only provides a ranking of the importance of influencing factors. Furthermore, previous studies typically considered natural emissions to be constant or excluded when training ML models to predict O_3 levels (Ning et al., 2024; Wang, Zhao, et al., 2023; Yin et al., 2022). However, natural emissions such as SNO_x and BVOCs strongly depend on the meteorological conditions, which can lead ML models to overemphasize the importance of other factors affecting O_3.

With the decline in anthropogenic emissions, further understanding the interaction between soil and ANO_x emissions and their impact on O_3 formation is crucial for developing more accurate mitigation strategies. In this study, we first reveal the long-term trends of O_3 during warm seasons (April–September) from 2010 to 2023 based on the ChinaHighO_3 data set (Wei et al., 2022), focusing on three key regions, that is, Beijing-Tianjin-Hebei (BTH), Fenwei Plain (FWP), and Yangtze River Delta (YRD) region. We then explain the reasons for the warm-season O_3 trend from the perspective of NO_x emission changes. Since the period from 2015 to 2019 is not affected by the COVID-19 pandemic and is more conducive to studying the quantitative impact of NO_x emissions changes on the long-term trend of O_3, these years are selected as the study period. The XGBoost model is chosen as the core framework for O_3 trend attribution, that is, to quantify the contribution of ANO_x and SNO_x to O_3 increase under declining anthropogenic emissions, which incorporates the dynamical natural emissions outputs from the UI-WRF-Chem model. Moreover, the UI-WRF-Chem model is applied to further verify whether the ML method could reliably quantify the response of O_3 pollution to emission changes. This study aims to assess the dynamic impacts of SNO_x on warm-season O_3 formation and develop dynamic O_3 mitigation strategies.

2. Materials and Methods

2.1. Observational Data of O_3 and Its Precursors

The hourly surface O_3 concentrations measurements at national monitoring sites for the period of 2014–2023 are obtained from the China National Environmental Monitoring Center (CNEMC) and converted to the maximum daily average 8-hr (MDA8) O_3 concentrations. Due to the lack of surface O_3 site observations before 2013 and the fact that CNEMC sites are mainly located in urban areas, while scarce in vast rural regions, we also incorporate the China High Air Pollutants (CHAP) data set developed by Wei et al. (2022) (CHAP: https://zenodo.org/records/13342827, last access: 1 December 2024). This data set employs a space-time extremely randomized tree (STET) model to estimate MDA8 O_3 concentrations (ChinaHighO_3) based on solar radiation intensity and surface temperature, combining ground-based observations, remote sensing products, atmospheric reanalysis, and an emission inventory. The spatial resolution is 1×1 km^2 and covers both urban and rural regions in China. Nighttime light data sets from DMSP/OLS (2010–2012) and NPP-VIIRS (2013–2023) with a spatial resolution of 500×500 m^2 (https://payneinstitute.mines.edu/eog/nighttime-lights/, last access: 1 December 2024) are used to dynamically distinguish the O_3 concentrations in urban and rural areas, employing a digital number (DN) threshold of 25 (Elvidge et al., 2021). This approach enables us to analyze the trends and distribution characteristics of O_3 in China from 2010 to 2023, covering the periods before and after the implementation of emission reduction policies and the COVID-19 pandemic.

The Ozone Monitoring Instrument (OMI) onboard NASA's Aura satellite was launched in 2004. It passes over the local area at around 13:45 local time (LT), with an orbital scanning width of 2,600 km and a spatial resolution of 13 km × 24 km (Levelt et al., 2006), and provides a global coverage once a day until 2007 and every two days thereafter (Dobber et al., 2006; Krotkov et al., 2017). The tropospheric columns of NO_2 from the OMI/Aura Level-3 NO_2 product (OMNO2d 003) with a spatial resolution of 0.25° × 0.25° for the period of 2015–2022 are used (https://disc.gsfc.nasa.gov/datasets/OMNO2d_003/summary?keywords=NO2, last access: 1 December 2024). The OMI NO_2 column product shows relatively high consistency with other satellite products. And the uncertainty depends on incomplete knowledge of the surface albedo, cloud and aerosol interference, and a priori NO_2 profile. Some of these uncertainties can be eliminated by averaging, and some persist when averaging over multiple pixels or over longer time periods (Glissenaar et al., 2025; Rijsdijk et al., 2025). Therefore, pixels with a cloud cover fraction below 30% and a solar zenith angle (SZA) less than 85% are selected for analysis. The total vertical column densities of HCHO are from the OMI/Aura Level-3 HCHO product (OMHCHOd 003), with a spatial resolution of 0.1° × 0.1° (https://disc.gsfc.nasa.gov/datasets/OMHCHOd_003/summary?keywords=HCHO, last access: 1 December 2024). The uncertainties in the OMHCHOd product are effectively controlled within 30% in polluted areas (González Abad et al., 2015; Li, Xu, et al., 2021; Rijsdijk et al., 2025). To ensure data quality and stability, pixels with a main data quality flag of 0, a cloud fraction below 30%, and an SZA less than 70% are selected. Since HCHO primarily exists in the troposphere, its total columns can be regarded as the tropospheric columns (Krotkov et al., 2017; Zhu et al., 2014).

2.2. Meteorology and Emission Data

The hourly meteorological data are from the fifth generation European Center for Medium-Range Weather Forecasts (ECMWF) atmospheric reanalysis of the global climate (ERA5, horizontal resolution of 0.1° × 0.1°, https://cds.climate.copernicus.eu/datasets/reanalysis-era5-land?tab=download). Among them, 2 m temperature (T2m, unit: K), 2 m dewpoint temperature (Td2m, unit: K), surface net solar radiation (Radiation, unit: J m^{-2}), 10m u-component and v-component of wind (U10, V10, unit: m s^{-1}), surface pressure (Press, unit: Pa), and total precipitation (Precp, unit: m) are used to train the XGBoost model.

The anthropogenic emissions of O_3 precursors in China are from the Multi-resolution Emission Inventory model for Climate and Air Pollution Research (MEIC) (http://meicmodel.org.cn, last access: 1 December 2024) (Geng et al., 2024; Li et al., 2017). The biogenic volatile organic compound (BVOCs) emissions calculated by the Model of Emissions of Gases and Aerosols from Nature (MEGAN) version v2.1 are from (Ma et al., 2021), which includes the hourly emission flux at a spatial resolution of 27 × 27 km^2 in China. There is a total of 19 emission species, including isoprene and terpenes derived from more than 100 emission compounds (Ma et al., 2019, 2021), and the BVOCs used to train the XGBoost model are the sum of all species. SNO_x are calculated using the Berkeley-Dalhousie-Iowa Soil NO Parameterization (BDISNP) coupled within the UI-WRF-Chem model. BDISNP is based on the BDSNP scheme and has undergone a series of improvements to enhance its applicability in the WRF-Chem model. The updated scheme has been successfully applied to quantitatively study the impact of SNO_x on O_3 pollution (Sha et al., 2021, 2024). Given the substantial impact of fertilizer nitrogen applications on SNO_x, and China has implemented a strategic shift since 2016 to reduce the utilization of nitrogen fertilizers and increase the application of compound fertilizers (Wang et al., 2024), we consider the temporal variations of both nitrogen fertilizers and compound fertilizers when calculating SNO_x by following the method of (Huang et al., 2023). Thus, unlike previous ML models for predicting O_3, our XGBoost model incorporates dynamically changing SNO_x and BVOCs.

2.3. Methods

2.3.1. Determination of O_3 Formation Regime

The most commonly used methods for identifying the O_3-NO_x-VOCs sensitivity include the observed photochemical indicators (e.g., O_3 production efficiency (OPE = $\Delta O_3/\Delta NO_z$) and H_2O_2/NO_z (or H_2O_2/HNO_3) ratio) and observation-based models (OBMs), which combine in situ field observations and chemical box models. However, ground-based measurements for photochemical indicators are often limited in temporal and spatial extent. Also, the OBM analysis requires measuring NO at sub-ppb levels and more than 50 different types of VOCs with high accuracy, which is difficult to achieve (Wang et al., 2017; Xue et al., 2014). Satellite remote sensing offers a valuable alternative way for investigating long-term periods of the O_3 formation regime on large spatial scales. It can provide continuous global observations on a daily basis for two indicative species of O_3 precursors, that is, NO_2 for NO_x (Chen et al., 2024; Travis et al., 2016) and formaldehyde (HCHO) for VOCs (Li, Jacob, et al., 2021; Liu, Tang, et al., 2020). NO_x can be approximated from the satellite observation of NO_2 columns because of the short lifetime of NO_x and high ratio of NO_2/NO_x in the planetary boundary layer (PBL) (Jin & Holloway, 2015; Johnson et al., 2024). Meanwhile, HCHO is an intermediate of the oxidation reaction of various VOCs in the atmosphere. The production of HCHO is approximately proportional to the summed rate of reactions of VOC with·OH radicals (Wang et al., 2010), and HCHO is also mainly concentrated within the PBL over polluted regions (Johnson et al., 2024). Therefore, HCHO can be used as a tracer for VOCs in the absence of other VOC observations (Chan et al., 2019; Duncan et al., 2010).

The satellite-based diagnostic method, that is, the ratio of HCHO to NO_2 columns (the Formaldehyde-to-NO_2 Ratio, FNR), has previously been proven to be highly consistent with the understanding of surface O_3 chemistry and is thus widely used as an effective indicator for determining the O_3 formation regimes (Chen et al., 2023; Cheng et al., 2019; Jin et al., 2020; Jin & Holloway, 2015; Wang, Zhao, et al., 2023). This method demonstrates robust consistency with other approaches in China, such as observed photochemical indicators and OBMs-based analysis (Cao et al., 2022; Lee et al., 2022; Li, Jacob, et al., 2021; Ren & Xie, 2022; Shen et al., 2021; Tong et al., 2023; Yuan et al., 2021). To investigate the long-term variation of O_3 formation regimes across different regions of China, we choose a satellite-based method to describe the surface O_3 formation regimes. Given that the overpass time of OMI satellite aligns with the peak period of O_3 photochemical formation, it serves as an optimal window for investigating O_3 formation regimes (Ren et al., 2021; Zhang et al., 2023). Concurrently, MDA8 O_3 is an indicator that characterizes the maximum daytime O_3 concentrations, which can thereby reflect the period of the strongest photochemical formation. Therefore, we integrate these two metrics, the FNR from OMI satellite observations and MDA8 O_3 concentrations from ChinaHighO_3 data set, to explore the long-term variations of O_3 formation regimes over three key regions (BTH, FWP, and YRD) of China during 2015–2022 (Chen et al., 2024; Wang, Zhao, et al., 2023).

The range of FNR values marking the transitional regime vary regionally and temporally (Schroeder et al., 2017). We follow the approach of Wang, Zhao, et al. (2023) and use nonlinear statistical models to examine the empirical relationship between O_3 formation and its precursors. To determine the FNR thresholds, we divide the satellite-based daily FNR during warm seasons from 2015 to 2022 into 200 intervals across different regions, calculate the 95th percentile of observed surface MDA8 O_3 concentrations for each FNR, and then evaluate their statistical relationship using a fourth-order polynomial model. Assuming the peak of the fitted curves represents the transition from VOCs-limited to NO_x-limited regimes, we define the transition regime as the FNR range corresponding to the top 20% of the MDA8 O_3 95th percentile distribution. The zone with FNR values below the minimum of this range is classified as the VOCs-limited regime, while those above the maximum value of this range are classified as the NO_x-limited regime. The zone with FNR values within this range is considered as mixed-limited regimes.

2.3.2. Machine Learning Model and Simulation Experiment Design

XGBoost is a supervised boosting algorithm that can effectively reduce the risk of overfitting, capture the nonlinear relationships among predictor variables, and provide rapid and accurate solutions to science problems (Chen & Guestrin, 2016). Compared with other bagging tree models, such as random forest, XGBoost can handle more complex data with fewer computing resources. It also has higher interpretability and computational efficiency than neural networks (Hu et al., 2017). Furthermore, it is less computationally expensive compared to the traditional CTMs, making it suitable for studying the long-term response of O_3 pollution to its precursors' emissions changes. To account for the spatiotemporal autocorrelation of O_3 and its covariates, the spatiotemporal information is also considered in the XGBoost model, including day of the year (DOY), longitude (Lon), and latitude (Lat) over the study domain. Both precipitation and emissions are processed as daily totals, while all other input variables are calculated as daily averages to maintain temporal consistency with the target variable, that is, MDA8 O_3. Bilinear interpolation and averaging are applied for upscaling and downscaling variables, respectively, to ensure a consistent spatial resolution of $0.1° \times 0.1°$ (Wang, Zhao, et al., 2023). Geographic locations with missing or invalid data for any day are excluded from the training data set to ensure data integrity and model reliability.

The XGBoost model for predicting MDA8 O_3 in this study is trained using 80% of the data from 2015 to 2019. The training data set included the following variables, that is, SNO_x, BVOCs emissions, anthropogenic emissions (including ANO_x and AVOCs), OMI NO_2 and HCHO columns, surface MDA8 O_3 and NO_2 concentrations from the ChinaHighO_3 and ChinaHighNO_2 data sets of CHAP, 7 meteorological variables from ERA5, and spatiotemporal variables (Lat, Lon, and DOY). The remaining 20% of the data is used to test the model (Figure 1). Correlation coefficients (R^2), root mean square error (RMSE), and mean absolute error (MAE) are used to evaluate model performance.

Quantifying the contribution of emission changes to long-term trends in O_3 pollution based on CTM methods requires high computing resources. The ML model provides an alternative approach, which is applied here. By using the trained XGBoost model, a series of sensitivity simulations are conducted to assess the impacts of changes in SNO_x and ANO_x from 2015 to 2019 on warm-season MDA8 O_3 concentrations. The descriptions of the sensitivity simulations are shown in Table 1. The O_3_2015 experiment is the MDA8 O_3 concentrations in 2015 predicted by the baseline XGBoost model. ΔO_3_ANO_x, ΔO_3_SNO_x, and ΔO_3_A + SNO_x represent the predicted O_3 concentrations when ANO_x, SNO_x, and both ANO_x and SNO_x are adjusted to the levels of 2016–2019, respectively. Comparing these three experiments results with O_3_2015, we can quantify the contribution of O_3 increases during this period caused by the change in NO_x emissions from 2016 to 2019 relative to 2015. Notably, due to the significant impacts of NO_x emissions on the atmospheric NO_2 budget, another XGBoost model is conducted to predict variations in NO_2 columns and surface concentrations resulting from NO_x emission changes (Table 2). The inputs of the model for predicting the changes in the NO_2 level here are exclusively constrained to ANO_x and SNO_x, and the baseline simulations predict the NO_2 columns and surface concentrations caused by

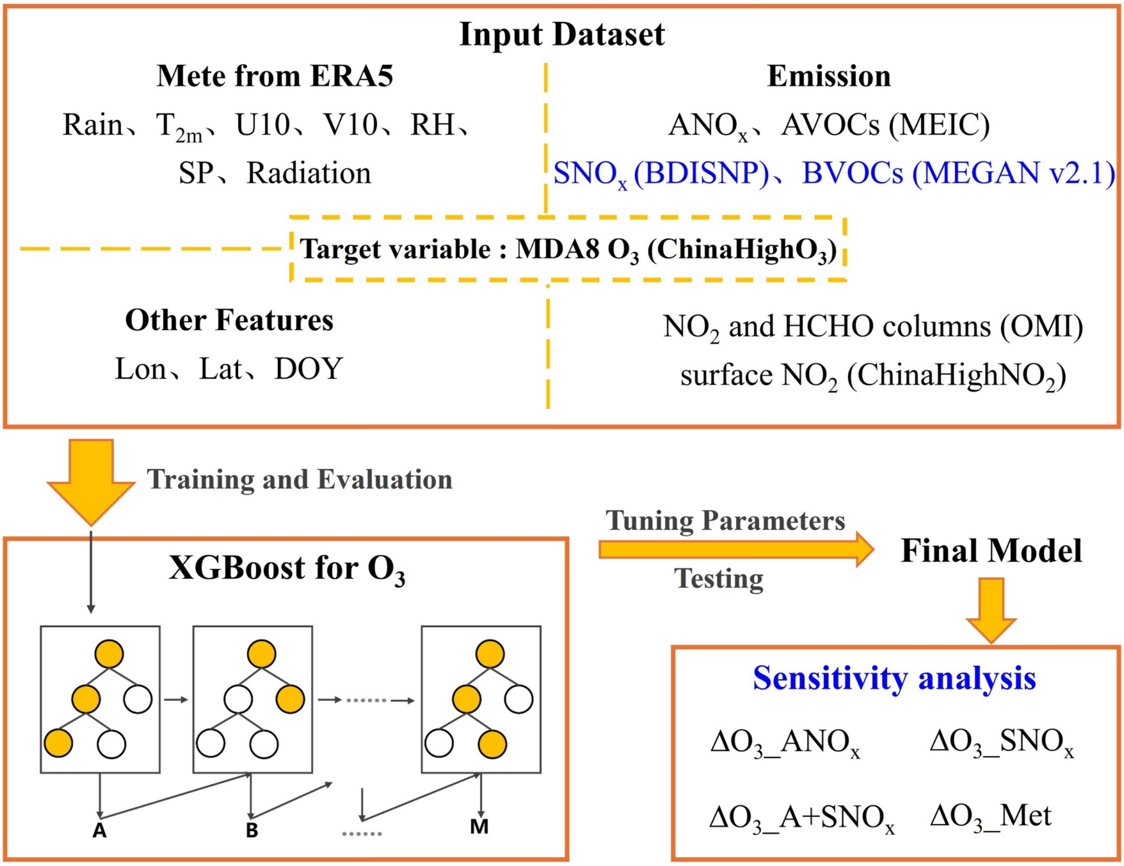

Figure 1. Flow diagram of quantifying the contribution of SNO_x changes to surface MDA8 O_3 concentrations using the XGBoost model.

emissions in 2015, denoted as NO_2VCD_2015 and NO_2_2015, respectively. Thus, the differences between the observations in 2015 and these simulations can be attributed to changes caused by other factors, represented as NO_2VCD_others and NO_2_others. Since only the changes in NO_x emissions are considered and all other factors are controlled at 2015 levels, we adjust ANO_x, SNO_x, and their combination to the levels of 2016–2019 for simulation, and the NO_2VCD_others (NO_2_others) are added into the simulation results to obtain the values of NO_2VCD_ANO_x (NO_2_ANO_x), NO_2VCD_SNO_x (NO_2_SNO_x), and NO_2VCD_A + SNO_x (NO_2_A + SNO_x) shown in Table 1. Additionally, the ΔO_3_Met experiment adjusts meteorological conditions to 2016–2019 levels while keeping NO_x emissions, NO_2 levels, and other factors at the year 2015. The difference between this experiment and O_3_2015 shows the O_3 variations due to the change in meteorological factors from 2016 to 2019 relative to 2015.

Table 1
Descriptions of the XGBoost Simulation Experiments for O_3 Response

Simulation	ANO_x	SNO_x	NO_2 VCD	NO_2	Met
O_3_2015	2015	2015	2015	2015	2015
ΔO_3_ANO_x	2016–2019	2015	NO_2VCD_ANO_x	NO_2_ ANO_x	2015
ΔO_3_SNO_x	2015	2016–2019	NO_2VCD_SNO_x	NO_2_ SNO_x	2015
ΔO_3_A + SNO_x	2016–2019	2016–2019	NO_2VCD_A + SNO_x	NO_2_ A + SNO_x	2015
ΔO_3_Met	2015	2015	2015	2015	2016–2019

Note. The other variables remain unchanged and remain at the year 2015.

Table 2
Descriptions of the XGBoost Simulation Experiments for the Changes in NO_2 Level

NO_2 VCD	ANO_x	SNO_x	Others	NO_2	ANO_x	SNO_x	Others
NO_2VCD_2015	2015	2015	—	NO_2_2015	2015	2015	—
NO_2VCD_ANO_x	2016–2019	2015	NO_2VCD_others	NO_2_ ANO_x	2016–2019	2015	NO_2_others
NO_2VCD_SNO_x	2015	2016–2019		NO_2_ SNO_x	2015	2016–2019	
NO_2VCD_A + SNO_x	2016–2019	2016–2019		NO_2_ A + SNO_x	2016–2019	2016–2019	

2.3.3. CTM and Simulation Experiment Design

We use the UI-WRF-Chem model to investigate the contribution of SNO_x to O_3 production and then validate the simulation performance of the XGBoost model. The 0.625° × 0.5° Modern-Era Retrospective analysis for Research and Applications, Version 2 (MERRA-2) reanalysis data provide the meteorological initial and boundary conditions. The 0.25° × 0.25° Global Land Data Assimilation System (GLDAS) data provide the initial and boundary conditions of soil properties (e.g., soil moisture and temperature), which have been shown to yield robust simulation performance (Bi et al., 2016; Zha et al., 2025). Details about the meteorological and chemical position data used in the UI-WRF-Chem and the improvements can be found in previous publications (Li, Wang, et al., 2024; Wang, Wang, et al., 2023). We conduct one domain simulation over China (67.5°–152.5°E, 9.4°–55.1°N) at a horizontal resolution of 27 km, with a grid dimension of 231 × 180 cells and 48 vertical levels from the surface to 50 hPa. Anthropogenic emissions are from the MEIC inventory. Biomass burning emissions are from the Fire INventory from NCAR (FINN, version 1.5, https://www.acom.ucar.edu/Data/fire/, last access: 1 December 2024). Biogenic emissions are calculated online using MEGAN v2.1. SNO_x are simulated with the improvement of using the BDISNP scheme (as described above). The selected physical and chemical schemes refer to our previous research (Sha et al., 2024). To explore the contribution of SNO_x on MDA8 O_3 concentrations, we conduct simulations for two scenarios in 2015 and 2019, that is, with SNO_x enabled (SNO_x) and with SNO_x disabled (NoSNO_x). The difference in MDA8 O_3 levels between these two scenarios quantifies the O_3 production driven specifically by SNO_x. The descriptions of the sensitivity simulations are given in Table 3.

3. Results and Discussions

3.1. O_3 Pollution Trends

The implementation of emission reduction strategies has reversed the increasing trend of ANO_x since 2011 (Figure S1 in Supporting Information S1). However, the observed warm-season MDA8 O_3 concentrations from CNEMC increased by 5.2 μg m^{-3} yr^{-1} from 2014 to 2023, with a notable increase during 2014–2017, a moderate decline during 2018–2020, and a slight rebound during the three-year COVID-19 pandemic period (2021–2023) (Figure S2a in Supporting Information S1). Additionally, the proportion of sites exceeding the World Health Organization (WHO) air quality guideline (MDA8 O_3 of 100 μg m^{-3}) increases from 2% in 2014 to 72% in 2023, with hotspots mainly located in eastern China (Figure S2b in Supporting Information S1). Since the monitoring sites from CNEMC are predominantly located in urban areas, it is difficult to comprehensively analyze O_3 pollution in suburban and rural regions, which cover a much larger area. Thus, we use the ChinaHighO_3 data set to evaluate the difference in O_3 pollution between urban and rural areas. Taking the year 2015 as an example, the monthly average relative bias between the MDA8 O_3 concentrations retrieved from the ChinaHighO_3 data set and the CNEMC observations ranges from 6% to 25%, with larger deviations in warm seasons compared to cold seasons (Figure S3 in Supporting Information S1). Overall, this data set exhibits high accuracy and provides reliable estimates of the monthly average MDA8 O_3 from 2013 to 2020, with R^2 of 0.93, RMSE of 9.42 μg m^{-3}, MAE of 6.91 μg m^{-3}, and mean relative error of 8.56% (Wei et al., 2022). This confirms the reliability of the ChinaHighO_3 data set in estimating O_3 concentrations and its capability to capture the long-term trends of O_3. The key regions, that is, BTH, FWP, and YRD, having severe O_3 pollution are selected to analyze the difference in O_3 pollution between urban and rural areas from 2010 to 2023. It includes four stages: before the implementation of the National Action Plan (2010–2012, Phase I), the first stage of Air Pollution

Table 3
Descriptions of the UI-WRF-Chem Simulation Experiments

Simulation	SNO_x	ANO_x	Others
SNO_x_15	2015	2015	2015
NoSNO_x_15	Turn off	2015	2015
SNO_x_19	2019	2019	2019
NoSNO_x_19	Turn off	2019	2019

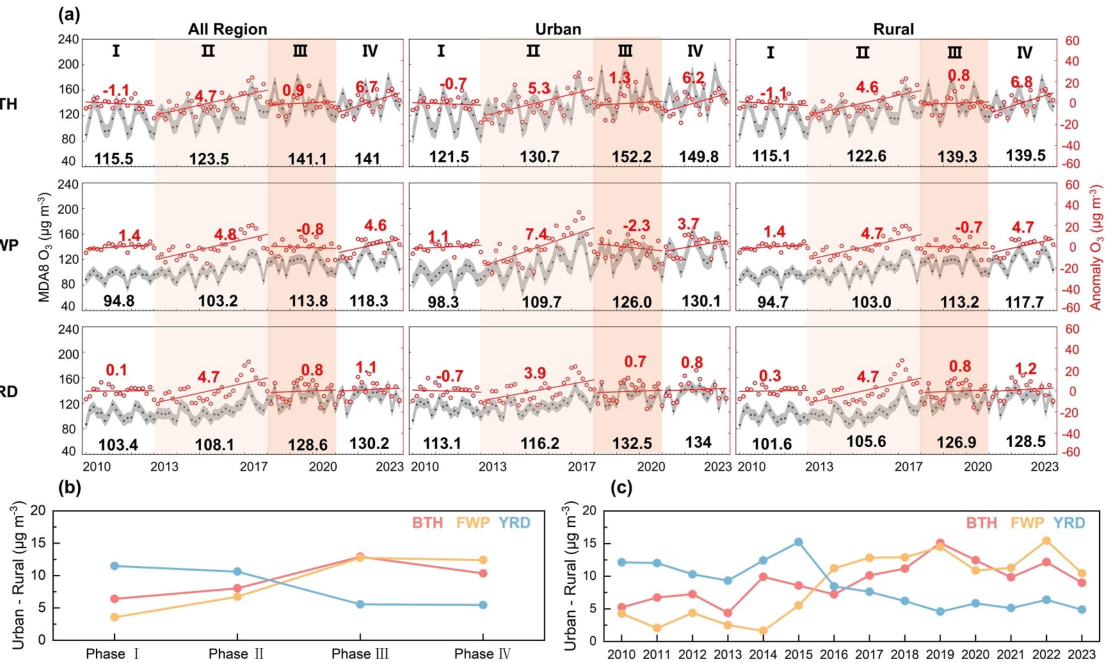

Figure 2. (a) Variation trends of monthly average MDA8 O_3 concentrations in the key regions during warm seasons from 2010 to 2023. The monthly averages of MDA8 O_3 in urban and rural areas of the three regions are black dots (left axis), and the anomalies are red circles (right axis). The monthly anomalies of MDA8 O_3 are defined as the difference between the monthly average of each individual month and the long-term monthly averages for the period 2010–2023. The gray shading represents the range of mean value ± the 50% standard deviation across all sites for each month. The black numbers denote the warm-season MDA8 O_3 averaged in each phase. The solid red line represents the linear fitting curve. (b) Urban-rural differences in MDA8 O_3 concentrations averaged during warm seasons in different stages. (c) Annual variation of urban-rural differences in MDA8 O_3 concentrations averaged during warm seasons.

Prevention and Control Action Plan (2013–2017, Phase II), the second stage of Air Pollution Prevention and Control Action Plan (2018–2020, Phase III), and the period from 2021 to 2023 (Phase IV).

Figure 2a shows that before the Chinese government implemented strict emission control measures for O_3 pollution, warm-season MDA8 O_3 concentrations remain relatively stable in Phase I. During Phase II, the reduction in ANO_x leads to O_3 increase, with the warm-season MDA8 O_3 increasing rate as high as 4.7–4.8 μg m^{-3} yr^{-1} across three key regions. Specifically, the increasing rate of MDA8 O_3 in urban areas of BTH is 5.3 μg m^{-3} yr^{-1}, and FWP is 7.4 μg m^{-3} yr^{-1}, both higher than that in rural areas (4.6 μg m^{-3} yr^{-1} for BTH and 4.7 μg m^{-3} yr^{-1} for FWP). In contrast, the YRD region shows the reverse trend, with rural MDA8 O_3 concentrations rising faster (4.7 μg m^{-3} yr^{-1}) than urban areas (3.9 μg m^{-3} yr^{-1}). In Phase III, MDA8 O_3 concentrations in the YRD and BTH regions continue to rise, though at a relatively moderate rate, while the FWP region exhibits a declining trend (−0.8 μg m^{-3} yr^{-1}). This may be related to the fact that AVOCs have been gradually brought under control, achieving a 6% reduction from 2018 to 2020 in China (Figure S1 in Supporting Information S1). Meteorological conditions also exert a negative influence on O_3 formation during this phase (Liu et al., 2023). For the Phase IV, O_3 pollution shows a significant rebound, likely driven by the effects of the three-year COVID-19 pandemic starting in 2020, during which substantial decreases in NO_x emissions from transportation increased oxidant levels (OH, HO_2, and NO_3), thereby enhancing the atmospheric oxidation capacity and accelerating O_3 production (Wang et al., 2021). Simultaneously, large-scale extreme heat events in central and eastern China in 2022 also offset the effectiveness of emission controls (Yan et al., 2024). In general, urban areas consistently exhibit higher warm-season MDA8 O_3 concentrations compared to rural areas. Urban-rural disparities in MDA8 O_3 are observed across all regions, with significant spatial heterogeneity (Figure 2b). The urban-rural gap shows an annual widening trend in the BTH and FWP while conversely narrowing in the YRD. Notably, rural MDA8 O_3 in all regions is progressively approaching or even exceeding the Grade II ambient air quality standard (160 μg m^{-3}). This indicates that O_3 pollution in agricultural areas requires more attention.

Since 2010, the O_3 pollution season (defined as MDA8 O_3 exceeding 160 μg m^{-3}) has gradually extended from summer to transitional seasons (spring and autumn), accompanied with an increasing frequency of O_3 pollution

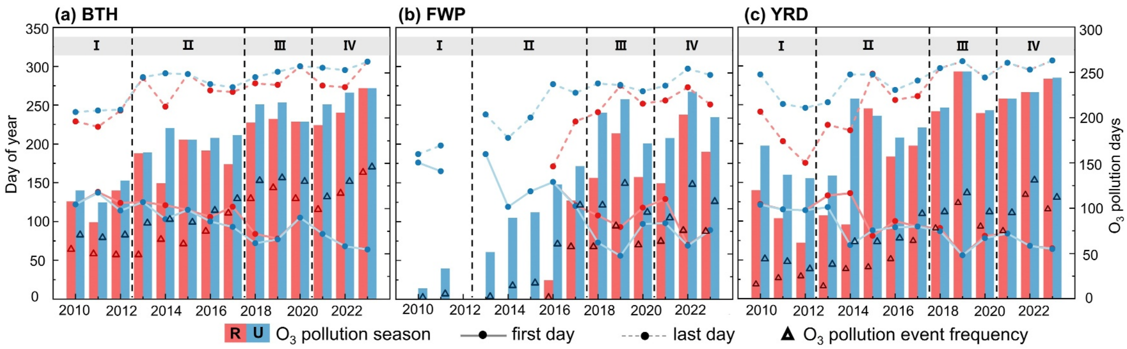

Figure 3. The season and frequency of O_3 pollution events in urban and rural areas of (a) BTH, (b) FWP, and (c) Yangtze River Delta regions from 2010 to 2023. The left axis corresponds to the lines, where solid and dashed lines denote the first and last occurrences of O_3 pollution, respectively. The right axis corresponds to the bars and triangular markers, which indicate the O_3 pollution season and event frequency, respectively. Red represents rural (R), and blue represents urban (U).

events (Figure 3). This trend is consistent with the previous study (Li, Jacob, et al., 2021), which revealed that the abrupt decrease of NO_x emissions over the North China Plain has not only led to increased O_3 concentrations in winter and spring but also extended the O_3 pollution events to span most of the year. The high frequency of springtime tropopause fold events promoting the transport of stratospheric O_3 into the troposphere may also lead to increased surface O_3 pollution (Lin et al., 2024; Luo et al., 2019). The turbulent entrainment by the deep convective boundary layer in the eastern plains is likely more effective at capturing descending lower-stratospheric air, contributing up to 16.7% to near-surface O_3 in eastern China during May–August 2019 via stratospheric intrusions (Meng et al., 2024). Additionally, the timing of O_3 pollution events is becoming more consistent between urban and rural areas in three major regions. Especially in the YRD region, the start and end dates of O_3 pollution in urban and rural areas have nearly coincided since 2019. Although rural areas have lower MDA8 O_3 concentrations and fewer pollution occurrences compared to urban areas, the areas affected by O_3 pollution are continuously expanding.

3.2. Changes in NO_x Emissions and NO_2 Columns

As one of the important precursors of O_3, NO_x emissions changes can affect O_3 formation. We compare the trends of NO_x emissions and NO_2 columns observed from OMI in the three key regions from 2015 to 2022 (including two pollution control phases) and normalized to the year 2015 (Figure S4 in Supporting Information S1). The implementation of air pollution control strategies leads to a steady decline in ANO_x, with anthropogenic emissions over the BTH, FWP, and YRD regions decreased by 11%, 24%, and 11% in 2020 compared to 2015, respectively (MEIC inventory is only available up to 2020). However, the variation of NO_2 columns shows a flattened decline trend during this period, and changes are −16% in BTH, −8% in FWP, and −8% in YRD. Although NO_2 columns are influenced not only by emissions but also by the ·OH concentrations (Shah et al., 2023), their slow variation suggests potential contributions from other sources. A mismatch between the decreasing rate of anthropogenic emissions and NO_2 columns has also been observed in regions such as the United States and Europe (Fortems-Cheiney et al., 2021; Jiang et al., 2022; Lu et al., 2015). This discrepancy has been attributed to changes in background emissions, particularly from soils and lightning sources (Silvern et al., 2019), a phenomenon further confirmed by increasing soil reactive nitrogen (Nr) emissions in rural China (Wang et al., 2024).

Figure 4 shows the simulated distribution of average warm-season SNO_x and ANO_x during 2015–2022. Note ANO_x from MEIC for the year 2021–2022 are set at the 2020 levels. It can be seen that in eastern China, where cities are densely concentrated, although ANO_x remain high, SNO_x are also substantial due to the extensive farmlands surrounding these urban areas. Across the entire region of China, warm-season SNO_x during this period account for a substantial proportion of the total NO_x emissions, with the proportion ranging from 23% to 27% (Figure S5 in Supporting Information S1). SNO_x are influenced by both soil properties, meteorological conditions, and fertilizer nitrogen applications. Despite a continued reduction in fertilizer application use across all provinces in China from 2015 to 2022 (Figure S6 in Supporting Information S1), the three key regions experienced significant warming during warm seasons: 2 m air temperatures increased at a rate of 0.1–0.2°C yr^{-1} and soil temperatures increased at a rate of 0.02–0.3°C yr^{-1} (Figure S7 in Supporting Information S1). This warming

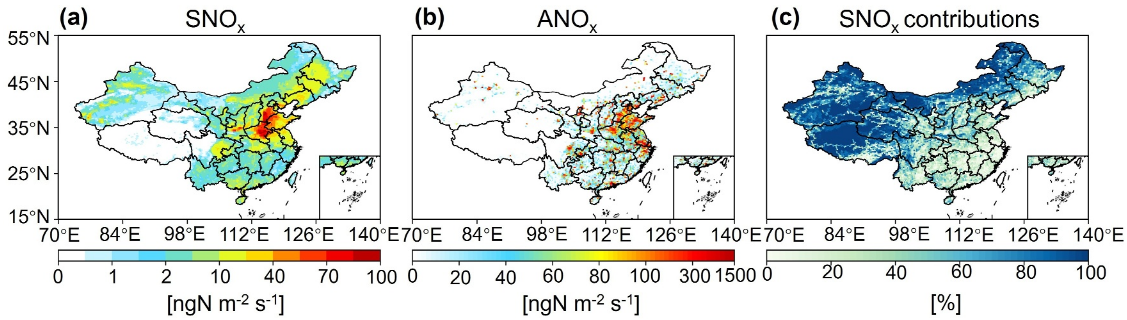

Figure 4. Distribution of the simulated average warm-season (a) SNO_x, (b) ANO_x, and (c) the contribution of SNO_x to total NO_x emissions in China during 2015–2022.

facilitates a shift of N cycling in terrestrial ecosystems from microbial immobilization to mineralization, nitrification, and denitrification, thereby promoting the production of SNO_x (Dai et al., 2020; Romer et al., 2018). Additionally, the intermittent soil pulses driven by soil dry-wet cycling further stimulate soil emissions to produce NO_x (Figure S8 in Supporting Information S1) (Dai et al., 2020; Oikawa et al., 2015; Wang et al., 2024), effectively offsetting SNO_x reductions resulting from the decreased fertilizer nitrogen use. As shown in Figure 5, in the years 2019 and 2022, the elevated temperatures and relatively dry soil conditions boost SNO_x across all three key regions. Overall, the decline in fertilizer nitrogen application, combined with rising temperatures and more frequent droughts, ultimately results in an increased proportion of SNO_x during both summer and transitional seasons in the FWP (from 28% to 31% in summer and from 21% to 24% in transitional seasons) and YRD (from 7% to 12% in summer and from 6% to 8% in transitional seasons) regions (Figures 5b and 5c). Although the proportion of SNO_x in the BTH shows a downward trend, it still accounts for more than 10% of total NO_x emissions (Figure 5a). These indicate that SNO_x play a significant role in total NO_x emissions, highlighting the urgent need to simultaneously control SNO_x.

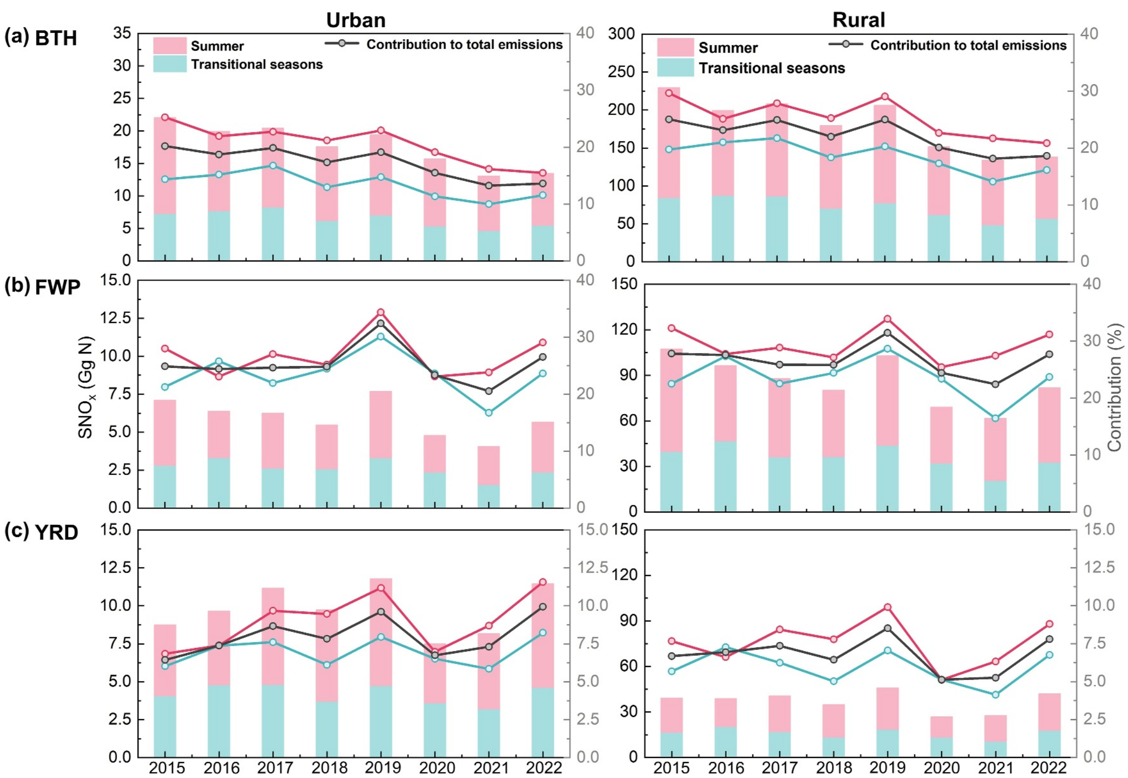

Figure 5. SNO_x (left axis) and their contribution to total NO_x emissions (right axis) during summer (pink), transitional season (green), and warm seasons (gray) from 2015 to 2022 in the BTH, FWP, and Yangtze River Delta regions.

We also study the changes in the sensitivity of O_3 formation to its precursors during the same period (2015–2022). We select the satellite-based FNR and MDA8 O_3 concentrations to explore the changes in the O_3 formation regime. A dynamic FNR threshold that changes with regions and seasons is also applied. In the FWP region, the FNR corresponding to the maximum of MDA8 O_3 concentrations in summer is 3.3, with a transitional range of 2.6–4.0, which is higher than that in the BTH region (2.2, 3.7) and the YRD region (2.1, 3.4) (Figure S9 in Supporting Information S1). Moreover, the FNR thresholds in summer for all regions are higher than those in the transitional seasons. This can be attributed to the increased air temperatures and stronger solar radiation, which promote plant growth, leading to increased BVOCs emissions and enhancing the photochemical reactions of VOCs (Li, Jacob, et al., 2021; Tanvir et al., 2024). The coverage of mixed and NO_x-limited regimes is expanding in the study regions (Figures S10–S13 in Supporting Information S1). During the transitional seasons, 23%, 7%, and 17% of the areas in the BTH, FWP, and YRD regions, respectively, transition from VOCs-limited to mixed-limited or NO_x-limited regimes. These regime shifts are more pronounced during the summer months, reaching 53%, 26%, and 22% in the BTH, FWP, and YRD regions, respectively. This may be mainly attributed to the reduction of ANO_x across all regions, while AVOCs remain relatively stable (Figure S1 in Supporting Information S1), thus making it easier for the FNR to shift toward mixed-limited and NO_x-limited regimes when the NO_x levels decrease. In addition, the increase in 2 m air temperature in summer (0.4–1.8°C) is more pronounced than that in the transitional seasons (0.1–1°C) during 2015–2022 (Tables S1 and S2 in Supporting Information S1), which may further promote the emission of BVOCs. The above suggests that the observed shifts in O_3 formation regimes, driven by the changing precursor levels and weather conditions, are a key factor in determining the characteristics of O_3 pollution.

3.3. Impacts of SNO_x on O_3 Increases

To further quantify the impact of SNO_x on long-term O_3 trends, the XGBoost models are separately developed for rural and urban areas in different regions. Although there are some differences in the performance of the models trained for different regions, the testing data set consistently shows good performance with an average coefficient of determination (R^2) of 0.93 (Figure S14 in Supporting Information S1). This indicates that these trained XGBoost models can accurately predict the spatiotemporal variability of O_3 concentrations in different regions. Figure 6a shows the contribution of changes in SNO_x and ANO_x from 2016 to 2019 to the increase in warm-season surface MDA8 O_3 in three key regions compared to the year 2015. These contributions are estimated by individually altering the meteorological conditions, SNO_x, and ANO_x. The changes in NO_2 columns and surface concentrations caused by the NO_x emission variations from 2016 to 2019 are also taken into account, and other nonvariable conditions are maintained at the year 2015 when simulating O_3. The meteorological factors dominated the MDA8 O_3 increases across all regions during 2016–2019, with elevating MDA8 O_3 by 2.6–22.2 μg m^{-3}, 5.9–19.0 μg m^{-3}, and 6.8–35.2 μg m^{-3} in the BTH, FWP, and YRD regions, respectively (Table S3 in Supporting Information S1). Although the contributions of changes in NO_x emissions to the increased MDA8 O_3 are much lower than meteorological factors (0.3–1.7 μg m^{-3} for the BTH, 1.4–13.0 μg m^{-3} for the FWP, and 1.1–2.1 μg m^{-3} for the YRD, respectively), it also has a positive contribution to the O_3 pollution. Due to the disparities of NO_x emission levels and their variations, as well as the O_3 formation regime across different regions, there are notable regional discrepancies in the response of MDA8 O_3 to NO_x emissions changes. For example, the promotion of O_3 enhancement by changes in NO_x emissions in urban areas of the FWP is more obvious compared to other regions, reaching 5.1–13.0 μg m^{-3}, which is comparable to the positive contribution from meteorological factors in this region. Additionally, in the urban areas of BTH and YRD regions, the reduction rates of ANO_x between 2015 and 2019 (−6% for the BTH and −13% for the YRD) are lower than the change in SNO_x (−12% for the BTH and 35% for the YRD). Therefore, the contribution of ANO_x changes to MDA8 O_3 increase during this period is relatively lower than that of SNO_x in urban areas, which is different from the situation in the FWP region.

We also evaluate the effect of changes in both ANO_x and SNO_x on O_3 increases. The MDA8 O_3 increases from total NO_x emissions changes (blue bar) are lower than the sum of individual contributions from each NO_x source (red bar). This illustrates that the interaction between NO_x emissions from anthropogenic and soils can suppress O_3 production from each source when either emission source changes. This nonlinear coupling effect results in an overall dampened sensitivity of O_3 photochemistry to NO_x perturbations (Tan et al., 2023). In contrast, the interaction between BVOCs and AVOCs is synergistic, as they jointly enhance O_3 formation by collectively increasing the availability of O_3 precursors (Gao et al., 2022).

10.1029/2025JD044623

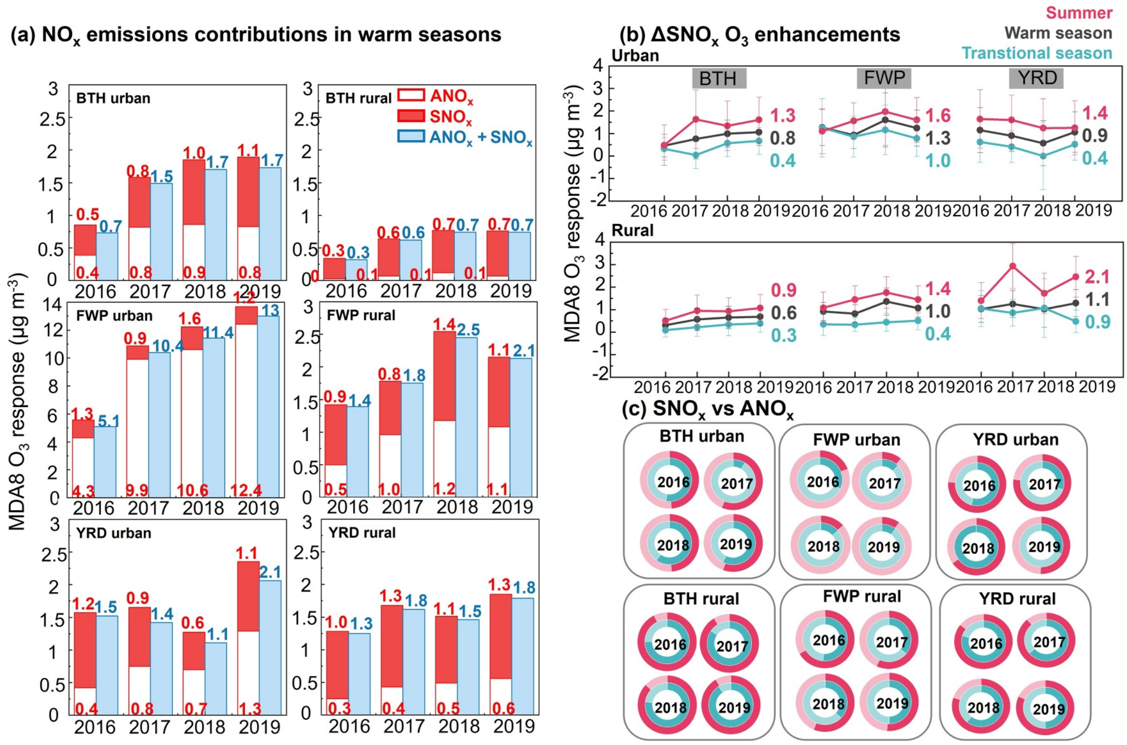

Figure 6. (a) Contribution of NO_x emission changes (SNO_x and ANO_x) to warm-season MDA8 O_3 concentrations in BTH, FWP, and Yangtze River Delta regions from 2016 to 2019 (relative to 2015). The bar chart shows the contributions of ANO_x (red hollow), SNO_x (red solid), and NO_x (SNO_x + ANO_x) (blue) to the MDA8 O_3 increase, respectively. (b) Contribution of SNO_x changes to MDA8 O_3 increase (i.e., ΔSNO_x O_3 enhancements) during warm seasons (gray), summer (pink), and transitional seasons (green) (unit: μg m^{-3}). The error bars are the range of mean value ±50% standard deviation across three regions for each season. The values in panels are the ΔSNO_x O_3 enhancements average in 2016–2019 during different seasons. (c) Relative contributions of SNO_x (dark shades) and ANO_x (light shades) to MDA8 O_3 during summer (pink) and transitional seasons (green) (unit: %).

As shown in Figure 6b, the increase in warm-season MDA8 O_3 caused by SNO_x changes (i.e., ΔSNO_x O_3 enhancements) has a gradual upward trend from 2015 to 2019 across all regions, except for the YRD region. For the BTH and FWP regions, despite higher SNO_x levels in the rural areas compared to the urban areas, the O_3 enhancements attributed to SNO_x changes in the rural areas are comparable or even smaller. Specifically, the range of warm-season ΔSNO_x O_3 enhancements from 2016 to 2019 in rural areas is 0.3–0.7 μg m^{-3} over BTH and 0.8–1.4 μg m^{-3} over FWP, while larger ΔSNO_x O_3 enhancements are found in the urban areas, with the range 0.5–1.1 μg m^{-3} for BTH and 0.9–1.6 μg m^{-3} for FWP. However, in the YRD region, the ΔSNO_x O_3 enhancements in rural areas (1.0–1.3 μg m^{-3}) are slightly greater than in urban areas (0.6–1.2 μg m^{-3}). These contrasting trends highlight the nonlinear response of O_3 to NO_x emissions. During warm seasons from 2015 to 2019, 7% of rural areas in the YRD region transition to NO_x-limited regimes (Table S4 in Supporting Information S1), and SNO_x increase by 17% (Figure S4c in Supporting Information S1). The transformation of sensitive regimes and the increase in SNO_x jointly promote O_3 formation. In contrast, urban areas primarily exhibit a transition from VOCs-limited to mixed-limited regimes. Although SNO_x levels increase more significantly in urban areas, the response of regional O_3 to SNO_x is weaker than in rural areas, where O_3 formation exhibits greater sensitivity to NO_x emissions due to dominant NO_x-limited and mixed-limited regimes. While regions like the BTH and FWP also experienced O_3 sensitivity regime shifts similar to the YRD, their urban areas retain strong VOCs-control characteristics, and thus a slight decrease in SNO_x could lead to an increase in O_3.

To further investigate the impact of SNO_x on the O_3 pollution season, we conduct a seasonal analysis of the simulation results for each region, focusing on summer and transitional seasons. It is worth noting that, compared with 2015, the summer (transitional-season) MDA8 O_3 concentrations increase by 0.5–1.6 (0–0.7) μg m^{-3} in BTH, 1.1–2.0 (0.3–1.3) μg m^{-3} in FWP, and 1.2–2.9 (0–1.1) μg m^{-3} in YRD regions during 2016–2019. From Figure 6b, the ΔSNO_x O_3 enhancements exhibit significant seasonal variations. During the summer months, elevated air temperatures and enhanced precipitation lead to much higher SNO_x compared to transitional seasons.

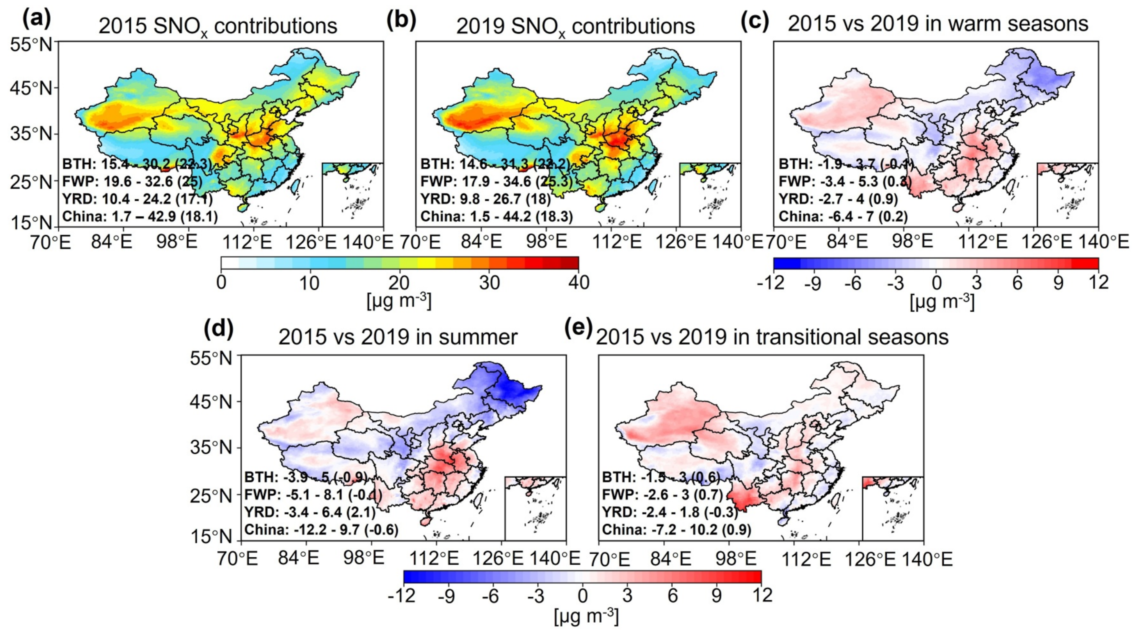

Figure 7. Simulated effects of SNO_x on warm-season MDA8 O_3 concentrations in (a) 2015 and (b) 2019 by the UI-WRF-Chem model. The changes in the MDA8 O_3 response to SNO_x between 2015 and 2019 during (c) warm seasons, (d) summer, and (e) transitional seasons. The numbers inserted in the figure represent the minimum and maximum values (average values) of the region.

In contrast, ANO_x remain relatively stable across warm seasons without significant variations. Consequently, SNO_x account for a larger proportion of NO_x emissions in summer and contribute more to regional O_3 concentrations than in transitional seasons. Specifically, from 2016 to 2019, summer average ΔSNO_x O_3 enhancements in urban (rural) areas are 1.3 (0.9) μg m^{-3}, 1.6 (1.4) μg m^{-3}, and 1.4 (2.1) μg m^{-3} for the BTH, FWP, and YRD regions, respectively, all of which are greater than that in transitional seasons, that is, 0.4 (0.3) μg m^{-3}, 1.0 (0.4) μg m^{-3}, and 0.4 (0.9) μg m^{-3} for the same regions. Except for the YRD, the ΔSNO_x O_3 enhancements in both summer and transitional seasons show an upward trend from 2016 to 2019 across the BTH and FWP regions. This indicates that the impact of SNO_x on O_3 pollution is not limited to the summer seasons. A recent study also provided robust evidence that agricultural fertilization drives the NO_2 columns increases (Wang et al., 2024). With the continuous decline in ANO_x, the role of fertilizer-induced SNO_x in O_3 formation during spring seasons will become increasingly significant. More attention should be paid to soil emissions caused by fertilization during transitional seasons in the future. The relative contributions of ANO_x and SNO_x to the O_3 increase are also evaluated. As shown in Figure 6c, the contribution of SNO_x to O_3 formation in rural areas can even exceed that of anthropogenic emissions, which SNO_x account for 84%–90%, 46%–65%, and 68%–81% of the total NO_x emissions-induced O_3 increases in the BTH, FWP, and YRD regions, respectively. Although the specific contributions vary by regions, SNO_x are consistently shown to promote MDA8 O_3 increases.

3.4. CTM-Based Validation

The UI-WRF-Chem model is utilized to validate the simulation results of ML model, specifically assessing the impact of SNO_x on the O_3 increase, and the traditional robust methods are applied for this validation. As shown in Figures 7a and 7b, the impacts of SNO_x on warm-season MDA8 O_3 during 2015 and 2019 are both consistently positive, with the values of 1.7–42.9 μg m^{-3} and 1.5–44.2 μg m^{-3}, respectively, indicating that the CTM based on physicochemical processes also confirms that the presence of SNO_x promotes O_3 formation. The contribution of SNO_x to surface O_3 production varies significantly across regions. In 2015, the contributions of SNO_x to MDA8 O_3 (i.e., SNO_x contributions) averaged in urban areas of the BTH and FWP regions are 23.8 μg m^{-3} and 27.1 μg m^{-3}, respectively, whereas those in rural areas are 22.0 μg m^{-3} and 24.9 μg m^{-3}. By 2019, the SNO_x contributions averaged in urban areas increase to 24.0 μg m^{-3} and 28.5 μg m^{-3}, and in rural areas, they change to 21.6 μg m^{-3} and 25.1 μg m^{-3}. Focusing on these 2 years, the contributions of SNO_x to MDA8 O_3 in urban areas are consistently slightly higher than those in rural areas, while the YRD region shows an opposite trend, where the

SNO_x contributions from urban and rural areas show no significant difference (Figure S15 in Supporting Information S1). The findings that BTH and FWP have a greater contribution of SNO_x to O_3 in urban areas align with the ML model results. Moreover, the sensitivity of regional O_3 formation to SNO_x shows distinct seasonal variations, with all regions exhibiting higher sensitivity in summer, which is also shown in the ML model results.

We also compared the changes in the response of MDA8 O_3 concentration to SNO_x between 2015 and 2019. Figures 7c–7e shows that the SNO_x contributions to O_3 formation during warm seasons in most regions of eastern China are greater in 2019 than in 2015. Among them, the changes in warm-season MDA8 O_3 caused by SNO_x are −3.4–5.3 μg m^{-3} (mean value: 0.3 μg m^{-3}) in the FWP and −2.7–4.0 μg m^{-3} (mean value: 0.9 μg m^{-3}) in YRD regions, while the response of warm-season MDA8 O_3 to SNO_x is not significant in the BTH region (−1.9–3.7 μg m^{-3}). Although the XGboost simulation results are slightly higher than the CTM results, with the changes in the warm-season MDA8 O_3 response to SNO_x from 2015 to 2019 being −1.5–10.0 μg m^{-3} (mean value: 0.7 μg m^{-3}) in BTH, −1.9–9.2 μg m^{-3} (mean value: 1.0 μg m^{-3}) in FWP, and −2.2–9.9 μg m^{-3} (mean value: 0.9 μg m^{-3}) in YRD regions (Figure S16 in Supporting Information S1), these ML models can still capture the promoting effect of warm-season SNO_x on O_3 increases. Additionally, the CTM results also indicate that the increase in the contributions of SNO_x to O_3 is more pronounced in summer than in the transitional seasons, further validating the accuracy of the conclusions from ML models regarding the seasonal differences in SNO_x contributions. The above findings demonstrate the ability of the XGBoost model to capture regional and seasonal variations of SNO_x contribution to O_3 pollution. Therefore, the data-driven ML model proved to be a powerful tool for quickly diagnosing the drivers of O_3 pollution.

4. Uncertainties

Uncertainties remain in our conclusion upon the integration of the classification of urban and rural areas, FNR threshold, NO_x emissions, and the XGBoost and WRF-Chem model simulation. First, the nighttime light data used to distinguish between urban and rural areas are resampled to 0.1° using an averaging method. Resampling high-resolution nighttime light data to a lower resolution could result in the loss of certain information, and the grid cells at this scale may, to some extent, obscure the boundaries of suburbs as an independent and distinct category (Hutchins et al., 2017). Moreover, applying a uniform standard for urban-rural division (DN threshold of 25) across different regions with varying levels of economic development also introduces certain uncertainties. However, since this study focuses on the quantitative results for the entire region rather than the individual grid cells, the potential misclassification of a small number of boundary cells is unlikely to significantly impact the overall conclusions. Future studies could enhance classification accuracy by integrating multiple indicators (e.g., land cover types, population density) for a comprehensive urban-rural assessment (Liu et al., 2017). Second, we employ a statistical modeling approach to determine the thresholds that describe transitions between different chemical regimes. These thresholds may be influenced by biases in satellite retrieval algorithms, and discrepancies between surface MDA8 O_3 concentrations and satellite-observed O_3 precursor columns, which may also vary depending on the specific O_3 metrics and fitting methods used. Third, there are uncertainties associated with NO_x emissions from both soils and anthropogenic emissions (MEIC). Fourth, due to the limited data for training and feature selection, the XGBoost model may not fully capture O_3 variations driven by SNO_x and other factors. Additionally, the discrepancy between the simulated MDA8 O_3 and the observations may also affect the evaluation of the role of SNO_x in O_3 mitigation strategies.

5. Conclusions

This study quantifies the impact of ANO_x and SNO_x on the increasing trend of MDA8 O_3 in urban and rural areas of eastern China from 2015 to 2019, based on the XGBoost model and further verified by the UI-WRF-Chem model, focusing on the three key regions (BTH, FWP, and YRD) because of high levels of O_3. From 2010 to 2023, the occurrence of O_3 pollution has gradually extended into transitional seasons (spring and autumn). Although rural areas have lower MDA8 O_3 and fewer pollution episodes compared to urban areas, the areas affected by O_3 pollution are gradually expanding. The decline rate of ANO_x is faster than satellited-based NO_2 columns, and this discrepancy indicates that as anthropogenic emissions decrease, natural sources, particularly the emissions from soils, exert a certain impact on the levels of NO_2 columns. We thus estimate the proportion of SNO_x in total NO_x emissions and find that their proportions vary between 23% and 27% during warm seasons from 2015 to 2022.

Results from the XGBoost model reveal that changes in SNO_x lead to MDA8 O_3 increases during 2015–2019 across all regions, with significant spatial and seasonal heterogeneity. In the urban areas of BTH and FWP, despite a reduction in VOCs-limited regimes, these regions still exhibit strong VOCs control characteristics; thus, a slight reduction in SNO_x leads to an increase in O_3. Specifically, compared with 2015, the urban MDA8 O_3 concentrations increase by 0.5–1.1 μg m^{-3} in BTH and 0.9–1.6 μg m^{-3} in FWP during warm seasons of 2016–2019. This increase exceeds those observed in the corresponding rural areas over the same period. However, in the YRD region, rural areas have primarily transitioned to a NO_x-limited regimes; thus, ΔSNO_x O_3 enhancements (1.0–1.3 μg m^{-3}) caused by increased SNO_x are slightly higher than in urban areas (0.6–1.2 μg m^{-3}). Furthermore, the response of O_3 to SNO_x changes is greater in summer than in the transitional seasons. Nevertheless, SNO_x can still promote the O_3 formation during transitional seasons, and the ΔSNO_x O_3 enhancements show an increasing trend from 2016 to 2019. Therefore, with the continued reduction of ANO_x, the sensitivity of O_3 formation to SNO_x is expected to increase. We also employ the UI-WRF-Chem model to independently validate these conclusions derived from the XGBoost. The CTM results show that the ML has the ability to quantify the contributions of driving factors such as specific emissions to O_3 pollution.

Our study emphasizes that despite lower SNO_x compared to anthropogenic emissions, they still pose a notable impact on the effectiveness of O_3 pollution mitigation. As anthropogenic emissions decrease, O_3 formation is likely to become more sensitive to SNO_x perturbations. Therefore, developing comprehensive O_3 pollution control strategies must consider the changes of both SNO_x and ANO_x and their impact on the O_3 formation, especially regional and seasonal differences in the sensitivity of O_3 formation to SNO_x. Meanwhile, the contribution of fertilization-driven SNO_x to O_3 formation in transitional seasons warrants more attention in future studies.

Conflict of Interest

The authors declare no conflicts of interest relevant to this study.

Data Availability Statement

The surface O_3 concentrations are obtained from the China National Environmental Monitoring Center (CNEMC) at https://quotsoft.net/air/ (last access: 1 December 2024). The China High Air Pollutants (CHAP) data set developed by Wei et al. (2022) is available at https://zenodo.org/records/13342827 (last access: 1 December 2024). OMI Level-3 data can be downloaded from the NASA Goddard Earth Sciences Data and Information Services Center (https://disc.gsfc.nasa.gov/datasets, last access: 1 December 2024). The anthropogenic emissions are available at the Multi-resolution Emission Inventory model for Climate and Air Pollution Research (MEIC) (http://meicmodel.org.cn, last access: 1 December 2024). The meteorological data are from the fifth generation European Center for Medium-Range Weather Forecasts (ECMWF) atmospheric reanalysis of the global climate (ERA5, https://cds.climate.copernicus.eu/datasets/reanalysis-era5-land?tab=download, last access: 1 December 2024). The source code of the trained XGBoost model for predicting MDA8 O_3 concentrations and NO_2 levels could be found in the Zenodo: https://zenodo.org/records/17096553. WRF-Chem is an open-access model and available at https://www2.mmm.ucar.edu/wrf/users/download/get_source.html (last access: 1 December 2024).

Acknowledgments

This study is supported by the National Natural Science Foundation of China (Grant 42205107) and the Shaanxi Key Laboratory of Environmental Monitoring and Forewarning of Trace Pollutions Open Fund Project (SHJKFJJYB-202409). Jun Wang's participation is made possible via the in-kind support from the University of Iowa.

References

Bi, H., Ma, J., Zheng, W., & Zeng, J. (2016). Comparison of soil moisture in GLDAS model simulations and in situ observations over the Tibetan Plateau. *Journal of Geophysical Research: Atmospheres*, *121*(6), 2658–2678. https://doi.org/10.1002/2015JD024131

Cao, J., Qiu, X., Liu, Y., Yan, X., Gao, J., & Peng, L. (2022). Identifying the dominant driver of elevated surface ozone concentration in North China Plain during summertime 2012–2017. *Environmental Pollution*, *300*, 118912. https://doi.org/10.1016/j.envpol.2022.118912

Chan, K. L., Wang, Z., Ding, A., Heue, K.-P., Shen, Y., Wang, J., et al. (2019). MAX-DOAS measurements of tropospheric NO_2 and HCHO in Nanjing and a comparison to ozone monitoring instrument observations. *Atmospheric Chemistry and Physics*, *19*(15), 10051–10071. https://doi.org/10.5194/acp-19-10051-2019

Chen, N., Yang, Y., Wang, D., You, J., Gao, Y., Zhang, L., et al. (2024). Changing ozone sensitivity in Fujian province, China, during 2012–2021: Importance of controlling VOC emissions. *Environmental Pollution*, *359*, 124757. https://doi.org/10.1016/j.envpol.2024.124757

Chen, T., & Guestrin, C. (2016). Xgboost: A scalable tree boosting system. In *Paper presented at proceedings of the 22nd acm sigkdd international conference on knowledge discovery and data mining*. https://doi.org/10.1145/2939672.2939785

Chen, Y., Wang, M., Yao, Y., Zeng, C., Zhang, W., Yan, H., et al. (2023). Research on the ozone formation sensitivity indicator of four urban agglomerations of China using ozone monitoring instrument (OMI) satellite data and ground-based measurements. *Science of the Total Environment*, *869*, 161679. https://doi.org/10.1016/j.scitotenv.2023.161679

Cheng, N., Li, R., Xu, C., Chen, Z., Chen, D., Meng, F., et al. (2019). Ground ozone variations at an urban and a rural station in Beijing from 2006 to 2017: Trend, meteorological influences and formation regimes. *Journal of Cleaner Production*, *235*, 11–20. https://doi.org/10.1016/j.jclepro.2019.06.204

Cheng, Y., Huang, X.-F., Peng, Y., Tang, M.-X., Zhu, B., Xia, S.-Y., & He, L.-Y. (2023). A novel machine learning method for evaluating the impact of emission sources on ozone formation. *Environmental Pollution*, *316*, 120685. https://doi.org/10.1016/j.envpol.2022.120685

Dai, Z., Yu, M., Chen, H., Zhao, H., Huang, Y., Su, W., et al. (2020). Elevated temperature shifts soil N cycling from microbial immobilization to enhanced mineralization, nitrification and denitrification across global terrestrial ecosystems. *Global Change Biology*, *26*(9), 5267–5276. https://doi.org/10.1111/gcb.15211

Ding, D., Xing, J., Wang, S., Dong, Z., Zhang, F., Liu, S., & Hao, J. (2021). Optimization of a NO_x and VOC cooperative control strategy based on clean air benefits. *Environmental Science & Technology*, *56*(2), 739–749. https://doi.org/10.1021/acs.est.1c04201

Dobber, M. R., Dirksen, R. J., Levelt, P. F., van den Oord, G. H., Voors, R. H., Kleipool, Q., et al. (2006). Ozone monitoring instrument calibration. *IEEE Transactions on Geoscience and Remote Sensing*, *44*(5), 1209–1238. https://doi.org/10.1109/TGRS.2006.869987

Duncan, B. N., Yoshida, Y., Olson, J. R., Sillman, S., Martin, R. V., Lamsal, L., et al. (2010). Application of OMI observations to a space-based indicator of NO_x and VOC controls on surface ozone formation. *Atmospheric Environment*, *44*(18), 2213–2223. https://doi.org/10.1016/j.atmosenv.2010.03.010

Elvidge, C. D., Zhizhin, M., Ghosh, T., Hsu, F.-C., & Taneja, J. (2021). Annual time series of global VIIRS nighttime lights derived from monthly averages: 2012 to 2019. *Remote Sensing*, *13*(5), 922. https://doi.org/10.3390/rs13050922

Fortems-Cheiney, A., Broquet, G., Pison, I., Saunois, M., Potier, E., Berchet, A., et al. (2021). Analysis of the anthropogenic and biogenic NO_x emissions over 2008–2017: Assessment of the trends in the 30 most populated urban areas in Europe. *Geophysical Research Letters*, *48*(11), e2020GL092206. https://doi.org/10.1029/2020GL092206

Gao, Y., Yan, F., Ma, M., Ding, A., Liao, H., Wang, S., et al. (2022). Unveiling the dipole synergic effect of biogenic and anthropogenic emissions on ozone concentrations. *Science of the Total Environment*, *818*, 151722. https://doi.org/10.1016/j.scitotenv.2021.151722

Geng, G., Liu, Y., Liu, Y., Liu, S., Cheng, J., Yan, L., et al. (2024). Efficacy of China's clean air actions to tackle $PM_{2.5}$ pollution between 2013 and 2020. *Nature Geoscience*, *17*(10), 987–994. https://doi.org/10.1038/s41561-024-01540-z

Glissenaar, I., Boersma, K. F., Anglou, I., Rijsdijk, P., Verhoelst, T., Compernolle, S., et al. (2025). TROPOMI level 3 tropospheric NO_2 dataset with advanced uncertainty analysis from the ESA CCI+ ECV precursor project. *Earth System Science Data Discussions*, *2025*, 1–36. https://doi.org/10.5194/essd-2024-616

González Abad, G., Liu, X., Chance, K., Wang, H., Kurosu, T., & Suleiman, R. (2015). Updated smithsonian astrophysical observatory ozone monitoring instrument (SAO OMI) formaldehyde retrieval. *Atmospheric Measurement Techniques*, *8*(1), 19–32. https://doi.org/10.5194/amt-8-19-2015

Hou, L., Dai, Q., Song, C., Liu, B., Guo, F., Dai, T., et al. (2022). Revealing drivers of haze pollution by explainable machine learning. *Environmental Science and Technology Letters*, *9*(2), 112–119. https://doi.org/10.1021/acs.estlett.1c00865

Hu, X., Belle, J. H., Meng, X., Wildani, A., Waller, L. A., Strickland, M. J., & Liu, Y. (2017). Estimating $PM_{2.5}$ concentrations in the conterminous United States using the random forest approach. *Environmental Science & Technology*, *51*(12), 6936–6944. https://doi.org/10.1021/acs.est.7b01210

Huang, L., Fang, J., Liao, J., Yarwood, G., Chen, H., Wang, Y., & Li, L. (2023). Insights into soil NO emissions and the contribution to surface ozone formation in China. *Atmospheric Chemistry and Physics*, *23*(23), 14919–14932. https://doi.org/10.5194/acp-23-14919-2023

Huang, L., Zhang, X., Emery, C., Mu, Q., Yarwood, G., Zhai, H., et al. (2025). Recommendations on benchmarks for numerical air quality model applications in China–Part 2: Ozone and uncertainty analysis. *Atmospheric Chemistry and Physics*, *25*(7), 4233–4249. https://doi.org/10.5194/acp-25-4233-2025

Huang, L., Zhu, Y., Zhai, H., Xue, S., Zhu, T., Shao, Y., et al. (2021). Recommendations on benchmarks for numerical air quality model applications in China–Part 1: $PM_{2.5}$ and chemical species. *Atmospheric Chemistry and Physics*, *21*(4), 2725–2743. https://doi.org/10.5194/acp-21-2725-2021

Huber, D. E., Steiner, A. L., & Kort, E. A. (2020). Daily cropland soil NOx emissions identified by TROPOMI and SMAP. *Geophysical Research Letters*, *47*(22), e2020GL089949. https://doi.org/10.1029/2020GL089949

Hutchins, M. G., Colby, J. D., Marland, G., & Marland, E. (2017). A comparison of five high-resolution spatially-explicit, fossil-fuel, carbon dioxide emission inventories for the United States. *Mitigation and Adaptation Strategies for Global Change*, *22*(6), 947–972. https://doi.org/10.1007/s11027-016-9709-9

Jiang, Z., Zhu, R., Miyazaki, K., McDonald, B. C., Klimont, Z., Zheng, B., et al. (2022). Decadal variabilities in tropospheric nitrogen oxides over United States, Europe, and China. *Journal of Geophysical Research: Atmospheres*, *127*(3), e2021JD035872. https://doi.org/10.1029/2021JD035872

Jin, X., Fiore, A., Boersma, K. F., Smedt, I. D., & Valin, L. (2020). Inferring changes in summertime surface Ozone–NO_x–VOC chemistry over US urban areas from two decades of satellite and ground-based observations. *Environmental Science & Technology*, *54*(11), 6518–6529. https://doi.org/10.1021/acs.est.9b07785

Jin, X., & Holloway, T. (2015). Spatial and temporal variability of ozone sensitivity over China observed from the ozone monitoring Instrument. *Journal of Geophysical Research: Atmospheres*, *120*(14), 7229–7246. https://doi.org/10.1002/2015jd023250

Johnson, M. S., Philip, S., Meech, S., Kumar, R., Sorek-Hamer, M., Shiga, Y. P., & Jung, J. (2024). Insights into the long-term (2005–2021) spatiotemporal evolution of summer ozone production sensitivity in the Northern hemisphere derived with the ozone monitoring instrument (OMI). *Atmospheric Chemistry and Physics*, *24*(18), 10363–10384. https://doi.org/10.5194/acp-24-10363-2024

Krotkov, N. A., Lamsal, L. N., Celarier, E. A., Swartz, W. H., Marchenko, S. V., Bucsela, E. J., et al. (2017). The version 3 OMI NO_2 standard product. *Atmospheric Measurement Techniques*, *10*(9), 3133–3149. https://doi.org/10.5194/amt-10-3133-2017

Kuo, C.-P., & Fu, J. S. (2023). Ozone response modeling to NO_x and VOC emissions: Examining machine learning models. *Environment International*, *176*, 107969. https://doi.org/10.1016/j.envint.2023.107969

Lee, H.-J., Chang, L.-S., Jaffe, D. A., Bak, J., Liu, X., Abad, G. G., et al. (2022). Satellite-based diagnosis and numerical verification of ozone formation regimes over nine megacities in East Asia. *Remote Sensing*, *14*(5), 1285. https://doi.org/10.3390/rs14051285

Levelt, P. F., Van Den Oord, G. H., Dobber, M. R., Malkki, A., Visser, H., De Vries, J., et al. (2006). The ozone monitoring instrument. *IEEE Transactions on Geoscience and Remote Sensing*, *44*(5), 1093–1101. https://doi.org/10.1109/TGRS.2006.872333

Li, C., Wang, J., Zhang, H., Diner, D. J., Hasheminassab, S., & Janechek, N. (2024). Improvement of surface $PM_{2.5}$ diurnal variation simulations in East Africa for the MAIA satellite mission. *ACS Es&t Air*, *1*(4), 223–233. https://doi.org/10.1021/acsestair.3c00008

Li, K., Jacob, D. J., Liao, H., Qiu, Y., Shen, L., Zhai, S., et al. (2021). Ozone pollution in the North China plain spreading into the late-winter haze season. *Proceedings of the National Academy of Sciences*, *118*(10), e2015797118. https://doi.org/10.1073/pnas.2015797118

Li, K., Jacob, D. J., Liao, H., Shen, L., Zhang, Q., & Bates, K. H. (2019). Anthropogenic drivers of 2013–2017 trends in summer surface ozone in China. *Proceedings of the National Academy of Sciences*, *116*(2), 422–427. https://doi.org/10.1073/pnas.1812168116

Li, K., Jacob, D. J., Liao, H., Zhu, J., Shah, V., Shen, L., et al. (2019). A two-pollutant strategy for improving ozone and particulate air quality in China. *Nature Geoscience*, *12*(11), 906–910. https://doi.org/10.1038/s41561-019-0464-x

Li, K., Jacob, D. J., Shen, L., Lu, X., De Smedt, I., & Liao, H. (2020). Increases in surface ozone pollution in China from 2013 to 2019: Anthropogenic and meteorological influences. *Atmospheric Chemistry and Physics*, *20*(19), 11423–11433. https://doi.org/10.5194/acp-20-11423-2020

Li, M., Liu, H., Geng, G., Hong, C., Liu, F., Song, Y., et al. (2017). Anthropogenic emission inventories in China: A review. *National Science Review*, *4*(6), 834–866. https://doi.org/10.1093/nsr/nwx150

Li, R., Xu, M., Li, M., Chen, Z., Gao, B., Zhao, N., & Yao, Q. (2021). Identifying the spatiotemporal variations of ozone formation regimes across China from 2005 to 2019 based on polynomial simulation and causality analysis. *Atmospheric Chemistry and Physics Discussions*, *2021*, 1–28. https://doi.org/10.5194/acp-21-15631-2021

Li, S., Gao, Y., Zhang, J., Hong, C., Zhang, S., Chen, D., et al. (2024). Mitigating climate change and ozone pollution will improve Chinese food security. *One Earth*, *8*(2), 101166. https://doi.org/10.1016/j.oneear.2024.12.002

Lin, Y., Tian, W., Xue, H., Luo, J., Zhang, J., Tian, H., & Liang, W. (2024). Global trends of tropopause folds in recent decades. *Atmospheric and Oceanic Science Letters*, *17*(3), 100450. https://doi.org/10.1016/j.aosl.2023.100450

Liu, F., Beirle, S., Zhang, Q., Van Der, A. R. J., Zheng, B., Tong, D., & He, K. (2017). NO_x emission trends over Chinese cities estimated from OMI observations during 2005 to 2015. *Atmospheric Chemistry and Physics*, *17*(15), 9261–9275. https://doi.org/10.5194/acp-17-9261-2017

Liu, R., Ma, Z., Liu, Y., Shao, Y., Zhao, W., & Bi, J. (2020). Spatiotemporal distributions of surface ozone levels in China from 2005 to 2017: A machine learning approach. *Environment International*, *142*, 105823. https://doi.org/10.1016/j.envint.2020.105823

Liu, Y., Geng, G., Cheng, J., Liu, Y., Xiao, Q., Liu, L., et al. (2023). Drivers of increasing ozone during the two phases of clean air actions in China 2013–2020. *Environmental Science & Technology*, *57*(24), 8954–8964. https://doi.org/10.1021/acs.est.3c00054

Liu, Y., Tang, Z., Abera, T., Zhang, X., Hakola, H., Pellikka, P., & Maeda, E. (2020). Spatio-temporal distribution and source partitioning of formaldehyde over Ethiopia and Kenya. *Atmospheric Environment*, *237*, 117706. https://doi.org/10.1016/j.atmosenv.2020.117706

Lu, X., Liu, Y., Su, J., Weng, X., Ansari, T., Zhang, Y., et al. (2025). Tropospheric ozone trends and attributions over east and Southeast Asia in 1995–2019: An integrated assessment using statistical methods, machine learning models, and multiple chemical transport models. *Atmospheric Chemistry and Physics*, *25*(14), 7991–8028. https://doi.org/10.5194/acp-25-7991-2025

Lu, X., Ye, X., Zhou, M., Zhao, Y., Weng, H., Kong, H., et al. (2021). The underappreciated role of agricultural soil nitrogen oxide emissions in ozone pollution regulation in North China. *Nature Communications*, *12*(1), 5021. https://doi.org/10.1038/s41467-021-25147-9

Lu, Z., Streets, D., De Foy, B., Lamsal, L., Duncan, B., & Xing, J. (2015). Emissions of nitrogen oxides from US urban areas: Estimation from ozone monitoring instrument retrievals for 2005–2014. *Atmospheric Chemistry and Physics*, *15*(18), 10367–10383. https://doi.org/10.5194/acp-15-10367-2015

Luo, J., Liang, W., Xu, P., Xue, H., Zhang, M., Shang, L., & Tian, H. (2019). Seasonal features and a case study of tropopause folds over the Tibetan Plateau. *Advances in Meteorology*, *2019*(1), 4375123. https://doi.org/10.1155/2019/4375123

Ma, M., Gao, Y., Ding, A., Su, H., Liao, H., Wang, S., et al. (2021). Development and assessment of a high-resolution biogenic emission inventory from urban green spaces in China. *Environmental Science & Technology*, *56*(1), 175–184. https://doi.org/10.1021/acs.est.1c06170

Ma, M., Gao, Y., Wang, Y., Zhang, S., Leung, L. R., Liu, C., et al. (2019). Substantial ozone enhancement over the north China plain from increased biogenic emissions due to heat waves and land cover in summer 2017. *Atmospheric Chemistry and Physics*, *19*(19), 12195–12207. https://doi.org/10.5194/acp-19-12195-2019

Ma, X., Huang, J., Zhao, T., Liu, C., Zhao, K., Xing, J., & Xiao, W. (2020). Rapid increase in summer surface ozone over the North China plain during 2013–2019: A side effect of particulate matters reduction control? *Atmospheric Chemistry and Physics Discussions*, *2020*, 1–30. https://doi.org/10.5194/acp-21-1-2021

Meng, K., Zhao, T., Bai, Y., Wu, M., Cao, L., Hou, X., et al. (2024). Tracing the origins of stratospheric ozone intrusions: Direct vs. indirect pathways and their impacts on central and eastern China in spring–summer 2019. *Atmospheric Chemistry and Physics*, *24*(22), 12623–12642. https://doi.org/10.5194/acp-24-12623-2024

Ni, Y., Yang, Y., Wang, H., Li, H., Li, M., Wang, P., et al. (2024). Contrasting changes in ozone during 2019–2021 between eastern and the other regions of China attributed to anthropogenic emissions and meteorological conditions. *Science of the Total Environment*, *908*, 168272. https://doi.org/10.1016/j.scitotenv.2023.168272

Ning, Z., Gao, S., Gu, Z., Ni, C., Fang, F., Nie, Y., et al. (2024). Prediction and explanation for ozone variability using cross-stacked ensemble learning model. *Science of the Total Environment*, *935*, 173382. https://doi.org/10.1016/j.scitotenv.2024.173382

Oikawa, P., Ge, C., Wang, J., Eberwein, J., Liang, L., Allsman, L., et al. (2015). Unusually high soil nitrogen oxide emissions influence air quality in a high-temperature agricultural region. *Nature Communications*, *6*(1), 8753. https://doi.org/10.1038/ncomms9753

Ren, J., Hao, Y., Simayi, M., Shi, Y., & Xie, S. (2021). Spatiotemporal variation of surface ozone and its causes in Beijing, China since 2014. *Atmospheric Environment*, *260*, 118556. https://doi.org/10.1016/j.atmosenv.2021.118556

Ren, J., & Xie, S. (2022). Diagnosing ozone-NO_x-VOC sensitivity and revealing causes of ozone increases in China based on 2013–2021 satellite retrievals. *Atmospheric Chemistry and Physics Discussions*, *2022*, 1–22. https://doi.org/10.5194/acp-22-15035-2022

Rijsdijk, P., Eskes, H., Dingemans, A., Boersma, K. F., Sekiya, T., Miyazaki, K., & Houweling, S. (2025). Quantifying uncertainties in satellite NO_2 superobservations for data assimilation and model evaluation. *Geoscientific Model Development*, *18*(2), 483–509. https://doi.org/10.5194/gmd-18-483-2025

Roelofs, G.-J., & Lelieveld, J. (1997). Model study of the influence of cross-tropopause O3 transports on tropospheric O_3 levels. *Tellus B: Chemical and Physical Meteorology*, *49*(1), 38–55. https://doi.org/10.3402/tellusb.v49i1.15949

Romer, P. S., Duffey, K. C., Wooldridge, P. J., Edgerton, E., Baumann, K., Feiner, P. A., et al. (2018). Effects of temperature-dependent NO_x emissions on continental ozone production. *Atmospheric Chemistry and Physics*, *18*(4), 2601–2614. https://doi.org/10.5194/acp-18-2601-2018

Schroeder, J. R., Crawford, J. H., Fried, A., Walega, J., Weinheimer, A., Wisthaler, A., et al. (2017). New insights into the column CH_2O/NO_2 ratio as an indicator of near-surface ozone sensitivity. *Journal of Geophysical Research: Atmospheres*, *122*(16), 8885–8907. https://doi.org/10.1002/2017JD026781

Sha, T., Ma, X., Zhang, H., Janechek, N., Wang, Y., Wang, Y., et al. (2021). Impacts of soil NO_x emission on O_3 air quality in rural California. *Environmental Science & Technology*, *55*(10), 7113–7122. https://doi.org/10.1021/acs.est.0c06834

Sha, T., Yang, S., Chen, Q., Li, L., Ma, X., Zhang, Y.-L., et al. (2024). Large contributions of soil emissions to the atmospheric nitrogen budget and their impacts on air quality and temperature rise in North China. *Atmospheric Chemistry and Physics*, *24*(14), 8441–8455. https://doi.org/10.5194/acp-24-8441-2024

Shah, V., Jacob, D. J., Dang, R., Lamsal, L. N., Strode, S. A., Steenrod, S. D., et al. (2023). Nitrogen oxides in the free troposphere: Implications for tropospheric oxidants and the interpretation of satellite NO_2 measurements. *Atmospheric Chemistry and Physics*, *23*(2), 1227–1257. https://doi.org/10.5194/acp-23-1227-2023

Shen, H., Sun, Z., Chen, Y., Russell, A. G., Hu, Y., Odman, M. T., et al. (2021). Novel method for ozone isopleth construction and diagnosis for the ozone control strategy of Chinese cities. *Environmental Science & Technology*, *55*(23), 15625–15636. https://doi.org/10.1021/acs.est.1c01567

Silvern, R. F., Jacob, D. J., Mickley, L. J., Sulprizio, M. P., Travis, K. R., Marais, E. A., et al. (2019). Using satellite observations of tropospheric NO_2 columns to infer long-term trends in US NO_x emissions: The importance of accounting for the free tropospheric NO_2 background. *Atmospheric Chemistry and Physics*, *19*(13), 8863–8878. https://doi.org/10.5194/acp-19-8863-2019

Tan, W., Wang, H., Su, J., Sun, R., He, C., Lu, X., et al. (2023). Soil emissions of reactive nitrogen accelerate summertime surface ozone increases in the North China plain. *Environmental Science & Technology*, *57*(34), 12782–12793. https://doi.org/10.1021/acs.est.3c01823

Tanvir, A., Javed, Z., Wang, S., Zhou, B., Zhang, S., & Bai, X. (2024). Vertical characteristics of HCHO and NO_2 in suburban Shanghai: Understanding of ozone formation sensitivity via secondary HCHO. *Environmental Research Letters*. https://doi.org/10.1088/1748-9326/ad2d3c

Tong, L., Liu, Y., Meng, Y., Dai, X., Huang, L., Luo, W., et al. (2023). Surface ozone changes during the COVID-19 outbreak in China: An insight into the pollution characteristics and formation regimes of ozone in the cold season. *Journal of Atmospheric Chemistry*, *80*(1), 103–120. https://doi.org/10.1007/s10874-022-09443-2

Travis, K. R., Jacob, D. J., Fisher, J. A., Kim, P. S., Marais, E. A., Zhu, L., et al. (2016). Why do models overestimate surface ozone in the Southeast United States? *Atmospheric Chemistry and Physics*, *16*(21), 13561–13577. https://doi.org/10.5194/acp-16-13561-2016

Vinken, G., Boersma, K., Maasakkers, J., Adon, M., & Martin, R. (2014). Worldwide biogenic soil NO_x emissions inferred from OMI NO_2 observations. *Atmospheric Chemistry and Physics*, *14*(18), 10363–10381. https://doi.org/10.5194/acp-14-10363-2014

Wang, C., Lin, J., Niu, Y., Wang, W., Wen, J., Lv, L., et al. (2022). Impact of ozone exposure on heart rate variability and stress hormones: A randomized-crossover study. *Journal of Hazardous Materials*, *421*, 126750. https://doi.org/10.1016/j.jhazmat.2021.126750

Wang, H., Huang, C., Tao, W., Gao, Y., Wang, S., Jing, S., et al. (2022). Seasonality and reduced nitric oxide titration dominated ozone increase during COVID-19 lockdown in eastern China. *Npj Climate and Atmospheric Science*, *5*(1), 24. https://doi.org/10.1038/s41612-022-00249-3

Wang, L., Zhao, Y., Shi, J., Ma, J., Liu, X., Han, D., et al. (2023). Predicting ozone formation in petrochemical industrialized Lanzhou city by interpretable ensemble machine learning. *Environmental Pollution*, *318*, 120798. https://doi.org/10.1016/j.envpol.2022.120798

Wang, Q., Wang, X., Huang, R., Wu, J., Xiao, Y., Hu, M., et al. (2022). Regional transport of $PM_{2.5}$ and O_3 based on complex network method and chemical transport model in the Yangtze River Delta, China. *Journal of Geophysical Research: Atmospheres*, *127*(5), e2021JD034807. https://doi.org/10.1029/2021JD034807

Wang, R., Bei, N., Wu, J., Li, X., Liu, S., Yu, J., et al. (2022). Cropland nitrogen dioxide emissions and effects on the ozone pollution in the North China Plain. *Environmental Pollution*, *294*, 118617. https://doi.org/10.1016/j.envpol.2021.118617

Wang, T., Xue, L., Brimblecombe, P., Lam, Y. F., Li, L., & Zhang, L. (2017). Ozone pollution in China: A review of concentrations, meteorological influences, chemical precursors, and effects. *Science of the Total Environment*, *575*, 1582–1596. https://doi.org/10.1016/j.scitotenv.2016.10.081

Wang, X., Wang, H., & Wang, S. (2010). Ambient formaldehyde and its contributing factor to ozone and OH radical in a rural area. *Atmospheric Environment*, *44*(17), 2074–2078. https://doi.org/10.1016/j.atmosenv.2010.03.023

Wang, Y., Wang, J., Zhang, H., Janechek, N., Wang, Y., Zhou, M., et al. (2023). Impact of land use change on the urban-rural temperature disparity in Eastern China. *Atmospheric Environment*, *308*, 119850. https://doi.org/10.1016/j.atmosenv.2023.119850

Wang, Y., Wang, Y., Li, Q., Tan, Y., Li, M., Zhang, Y., et al. (2024). Soil emissions of reactive oxidized nitrogen reduce the effectiveness of anthropogenic source control in China. *Environmental Science & Technology*, *58*(47), 21015–21024. https://doi.org/10.1021/acs.est.4c08526

Wang, Y., Zhao, Y., Liu, Y., Jiang, Y., Zheng, B., Xing, J., et al. (2023). Sustained emission reductions have restrained the ozone pollution over China. *Nature Geoscience*, *16*(11), 967–974. https://doi.org/10.1038/s41561-023-01284-2

Wang, Y., Zhu, S., Ma, J., Shen, J., Wang, P., Wang, P., & Zhang, H. (2021). Enhanced atmospheric oxidation capacity and associated ozone increases during COVID-19 lockdown in the Yangtze River Delta. *Science of the Total Environment*, *768*, 144796. https://doi.org/10.1016/j.scitotenv.2020.144796

Wei, J., Li, Z., Li, K., Dickerson, R. R., Pinker, R. T., Wang, J., et al. (2022). Full-coverage mapping and spatiotemporal variations of ground-level ozone (O_3) pollution from 2013 to 2020 across China. *Remote Sensing of Environment*, *270*, 112775. https://doi.org/10.1016/j.rse.2021.112775

Xue, L., Wang, T., Gao, J., Ding, A., Zhou, X., Blake, D., et al. (2014). Ground-level ozone in four Chinese cities: Precursors, regional transport and heterogeneous processes. *Atmospheric Chemistry and Physics*, *14*(23), 13175–13188. https://doi.org/10.5194/acp-14-13175-2014

Yan, D., Jin, Z., Zhou, Y., Li, M., Zhang, Z., Wang, T., et al. (2024). Anthropogenically and meteorologically modulated summertime ozone trends and their health implications since China's clean air actions. *Environmental Pollution*, *343*, 123234. https://doi.org/10.1016/j.envpol.2023.123234

Yan, X., Ohara, T., & Akimoto, H. (2005). Statistical modeling of global soil NO_x emissions. *Global Biogeochemical Cycles*, *19*(3). https://doi.org/10.1029/2004GB002276

Yang, Y., Zhou, Y., Wang, H., Li, M., Li, H., Wang, P., et al. (2024). Meteorological characteristics of extreme ozone pollution events in China and their future predictions. *Atmospheric Chemistry and Physics*, *24*(2), 1177–1191. https://doi.org/10.5194/acp-24-1177-2024

Yao, T., Lu, S., Wang, Y., Li, X., Ye, H., Duan, Y., et al. (2024). Revealing the drivers of surface ozone pollution by explainable machine learning and satellite observations in Hangzhou Bay, China. *Journal of Cleaner Production*, *440*, 140938. https://doi.org/10.1016/j.jclepro.2024.140938

Yin, H., Sun, Y., Notholt, J., Palm, M., Ye, C., & Liu, C. (2022). Quantifying the drivers of surface ozone anomalies in the urban areas over the Qinghai-Tibet Plateau. *Atmospheric Chemistry and Physics*, *22*(21), 14401–14419. https://doi.org/10.5194/acp-22-14401-2022

Yuan, Q., Qi, B., Hu, D., Wang, J., Zhang, J., Yang, H., et al. (2021). Spatiotemporal variations and reduction of air pollutants during the COVID-19 pandemic in a megacity of Yangtze River Delta in China. *Science of the Total Environment*, *751*, 141820. https://doi.org/10.1016/j.scitotenv.2020.141820

Zha, X., Jia, S., Han, Y., Zhu, W., & Lv, A. (2025). Enhancing soil moisture prediction in drought-prone agricultural regions using remote sensing and machine learning approaches. *Remote Sensing*, *17*(2), 181. https://doi.org/10.3390/rs17020181

Zhang, L., Wang, L., Ji, D., Xia, Z., Nan, P., Zhang, J., et al. (2024). Explainable ensemble machine learning revealing the effect of meteorology and sources on ozone formation in megacity Hangzhou, China. *Science of the Total Environment*, *922*, 171295. https://doi.org/10.1016/j.scitotenv.2024.171295

Zhang, X., Xu, W., Zhang, G., Lin, W., Zhao, H., Ren, S., et al. (2022). Discrepancies in ozone levels and temporal variations between urban and rural North China plain: Possible implications for agricultural impact assessment across China. *Elem Sci Anth*, *10*(1), 00019. https://doi.org/10.1525/elementa.2022.00019

Zhang, Y., Shi, M., Chen, J., Fu, S., & Wang, H. (2023). Spatiotemporal variations of NO_2 and its driving factors in the coastal ports of China. *Science of the Total Environment*, *871*, 162041. https://doi.org/10.1016/j.scitotenv.2023.162041

Zhang, Y., Yu, S., Chen, X., Li, Z., Li, M., Song, Z., et al. (2022). Local production, downward and regional transport aggravated surface ozone pollution during the historical orange-alert large-scale ozone episode in eastern China. *Environmental Chemistry Letters*, *20*(3), 1577–1588. https://doi.org/10.1007/s10311-022-01421-0

Zhu, J.-J., Yang, M., & Ren, Z. J. (2023). Machine learning in environmental research: Common pitfalls and best practices. *Environmental Science & Technology*, *57*(46), 17671–17689. https://doi.org/10.1021/acs.est.3c00026

Zhu, L., Jacob, D. J., Mickley, L. J., Marais, E. A., Cohan, D. S., Yoshida, Y., et al. (2014). Anthropogenic emissions of highly reactive volatile organic compounds in eastern Texas inferred from oversampling of satellite (OMI) measurements of HCHO columns. *Environmental Research Letters*, *9*(11), 114004. https://doi.org/10.1088/1748-9326/9/11/114004